Volume 39
DOE/DP40200-95

LLE Review

Quarterly Report

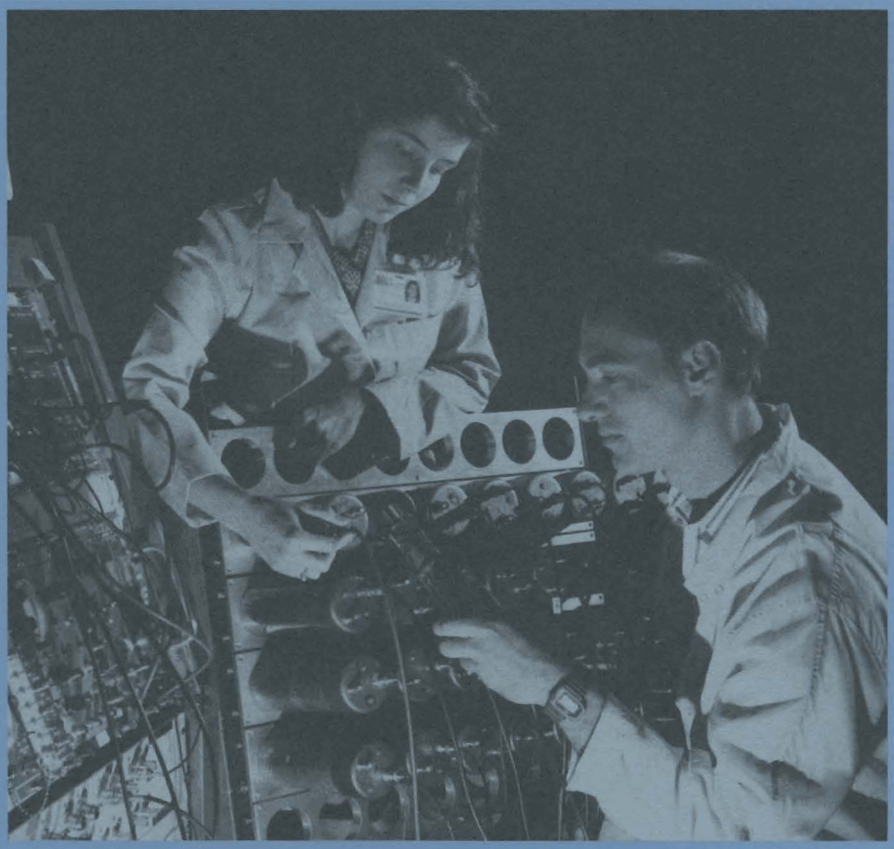

April–June 1989

Laboratory for Laser Energetics
College of Engineering and Applied Science
University of Rochester
250 East River Road
Rochester, New York 14623-1299

Volume 39
DOE/DP40200-95

LLE Review

Quarterly Report

Editor: A. Simon
(716) 275-7703

April–June 1989

Laboratory for Laser Energetics
College of Engineering and Applied Science
University of Rochester
250 East River Road
Rochester, New York 14623-1299

IN BRIEF

This volume of the LLE Review, covering the period April–June 1989, includes the second part of a two-part series dealing with the preliminary design of the OMEGA Upgrade. One article provides a general overview of the current upgrade system configuration and another article describes the target system. Future issues of the LLE Review will cover other aspects of the OMEGA Upgrade as the detailed system design develops. In addition, the advanced technology section of this issue contains an article discussing the interaction of a picosecond optical pulse with high-temperature superconductors. Finally, the activities of the National Laser Users Facility and the GDL and OMEGA laser facilities are summarized.

The following are highlights of the research reports contained in this issue:

- The preliminary design of the OMEGA Upgrade is near completion. A viable concept has been established, and areas requiring further development have been identified.

- A study has been carried out of the radiological effects on the target chamber and surrounding area that would result from a maximum-credible neutron yield, and shielding requirements have been estimated.

- A 150-ps optical pulse has been shown to induce a very rapid transition from the superconducting to the usual state, in a high-temperature superconducting film. Switching back to the superconducting state tends to be much slower.

CONTENTS

Page

IN BRIEF iii

CONTENTS v

Section 1 THE OMEGA UPGRADE 113
Part II: Preliminary Design and Target System 113
1.A OMEGA Upgrade Preliminary Design 114
1.B Target Experimental System 133

Section 2 ADVANCED TECHNOLOGY DEVELOPMENTS 151
2.A Interaction of Picosecond Optical Pulse with High-Temperature Superconductors 151

Section 3 NATIONAL LASER USERS FACILITY NEWS 161

Section 4 LASER SYSTEM REPORT 163
4.A GDL Facility Report 163
4.B OMEGA Facility Report 164

PUBLICATIONS AND CONFERENCE PRESENTATIONS

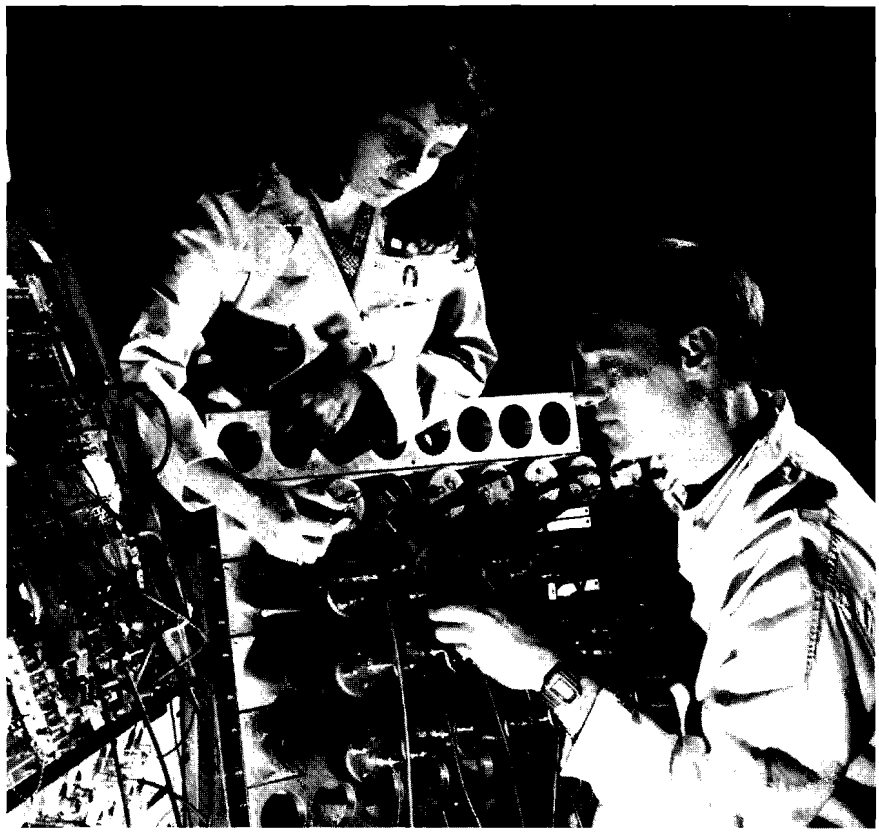

Marie Russotto, Research Engineer, and Bob Kremens, Scientist, are shown assembling a 32-channel, single-hit neutron time-of-flight detector. This device will measure neutron yield and spectra, and will serve as the prototype for a larger detector planned for the OMEGA Upgrade.

Section 1
THE OMEGA UPGRADE

Part II: Preliminary Design and Target System

In the first article of this issue we present a description of the preliminary design of the OMEGA Upgrade, which is now near completion. This design has evolved significantly over the past two years as a result of numerous reviews, efforts to control costs, the elimination of unnecessary complexity, and the development of smoothing by spectral dispersion (SSD). For example, the multisegmented amplifiers described in the last issue of the LLE Review have been replaced with disk amplifiers of conventional design, and the location of the frequency-conversion crystals has been changed from the target-mirror structure to the laser bay.

We have now converged upon a basic concept that will provide the laser energy, uniformity, and pulse shape needed to enable LLE to carry out an important series of ignition-scaling experiments in the 1990s. We have also identified portions of the preliminary design where further theoretical and experimental investigations and prototyping are necessary before arriving at the final design.

In the second article we describe the target system of the OMEGA Upgrade, including the experimental target chamber, the target-positioning and viewing systems, the vacuum system, and the target diagnostic systems. In addition, we report the results of a study carried out with Grumman Aerospace of possible radiological effects on the target chamber and the surrounding area.

1.A OMEGA Upgrade Preliminary Design

In this article we give a general description of the baseline design for the OMEGA Upgrade, including its motivation, capabilities, and limitations. We start by showing how the theoretical desire for a shaped pulse, coupled with the practical limitations inherent in the third-harmonic-generation process, leads to a co-propagated main-pulse/foot-pulse system, and how the parameters of the desired UV pulse on target lead to requirements imposed on the IR portion of the system. These considerations also lead to the anticipated performance parameters of the system. We then proceed to give a brief description of each of the main subsystems, working from the oscillators to the target chamber. We include a discussion of some physical processes, such as laser-beam propagation, stimulated rotational Raman scattering, and transverse stimulated Brillouin scattering, and show that these processes do not adversely affect the viability of the upgrade design.

Number of Beams and Pulse Shaping

A key parameter is the number of beams on target. For direct drive, this number is by no means arbitrary if a reasonably symmetric structure in the target area is desired. Given any number of beams (N), we can use a computer code (REPEL) to find a reasonable placement configuration by treating the beams as identical point charges on a sphere and minimizing their potential energy; however, with the exception of a small set of values of N, this does not yield solutions with adequate symmetry. The most practical configurations are based on subdivisions of the Platonic solids: e.g., placing four beams on each face of the cube gives the current OMEGA configuration; placing one beam on each vertex and face of a dodecahedron (or equivalently an icosahedron) gives a 32-beam configuration (known as a truncated icosahedron), which maps on to the 32 faces of a soccer ball; and placing one beam at each vertex of a soccer ball (5 for each of the 12 pentagonal faces) yields a symmetrical 60-beam configuration where all beams are equivalent; combining the 32 faces and 60 vertices of the soccer ball gives a 92-beam configuration, and so on. We have adopted the 60-beam configuration as it provides significant additional uniformity over the existing 24-beam system for minimum additional complexity. [We do not claim originality: the tobacco necrosis virus, for example, is a simple shell of 60 identical protein molecules,[1] and the same structure has been proposed for a molecule containing 60 carbon atoms ("buckminsterfullerene").[2]] It is also important to note that the beam aperture required to supply 30 kJ in 60 beamlines is sufficiently small that segmentation can be avoided, and use can be made of optical components having a reasonably low cost-per-unit area.

The detailed 60-beam irradiation geometry selected is shown in Fig. 39.1, and referred to as a "stretched-soccer-ball" configuration. This is arrived at by first placing five beams at the corners of each of the 12

pentagonal faces of a soccer ball, and then adjusting the one free parameter in this geometry, namely the distance of a beam from the center of a pentagon. This distance is increased slightly from that corresponding to the ideal soccer-ball geometry, such that the distance between neighboring beams measured around a pentagonal face (A in Fig. 39.1) is a factor of 1.2 greater than the distance B on a hexagonal face. The hexagonal faces are no longer truly hexagonal, but irradiation uniformity is improved because clustering around the pentagonal faces is eliminated. This geometry provides enough uniformity to meet the theoretical on-target uniformity requirement of 1%–2% rms, but there are not so many beams that the system is too complex to be viable.

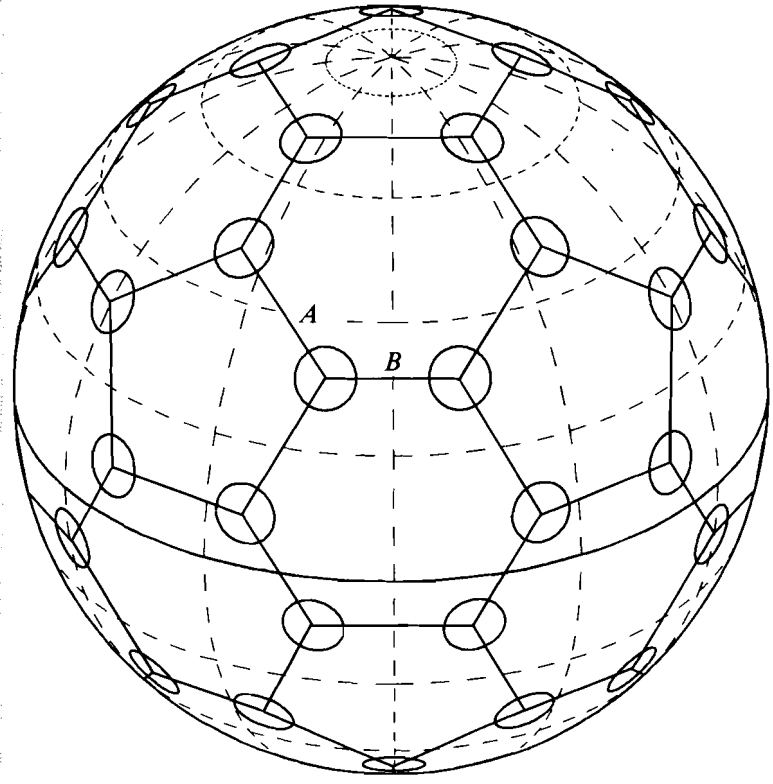

Fig. 39.1
60-beam stretched-soccer-ball geometry proposed for the OMEGA Upgrade.

Generation of the shaped pulse required for an efficient ablative target implosion presents a significant problem because of the limited dynamic range of all known practical frequency-tripling schemes: quadrature schemes[3] permit high-dynamic-range frequency doubling

but not tripling, while the polarization-bypass tripling scheme,[4] which has an unlimited dynamic range, is too sensitive to misalignment to be practical for use with KDP. It is useful to approximate the ideal shaped pulse [shown dashed in Fig. 39.2(a)] as the sum of two Gaussians, a "foot" pulse followed by a "main" pulse: in practice, pulse-shaping techniques can be applied to these Gaussians to provide a closer approximation to the dashed curve, especially around the time that the two pulses merge. The peak powers of the foot and main pulses are typically in a ratio of 1:20. One option is to select the frequency-conversion crystals to provide efficient tripling of the main pulse, and compensate for low tripling efficiency in the foot pulse by generating extra infrared energy in the foot; however, this is wasteful of laser energy. Another option is to build separate laser systems for the two pulses, from the oscillator to the focusing lenses, but this would entail considerable extra complexity and additional cost, especially around the target chamber.

Co-propagation

The solution that has been incorporated into the upgrade design is a co-propagated laser,[5] in which a small-diameter foot pulse of cylindrical cross section propagates inside an annular main pulse [see

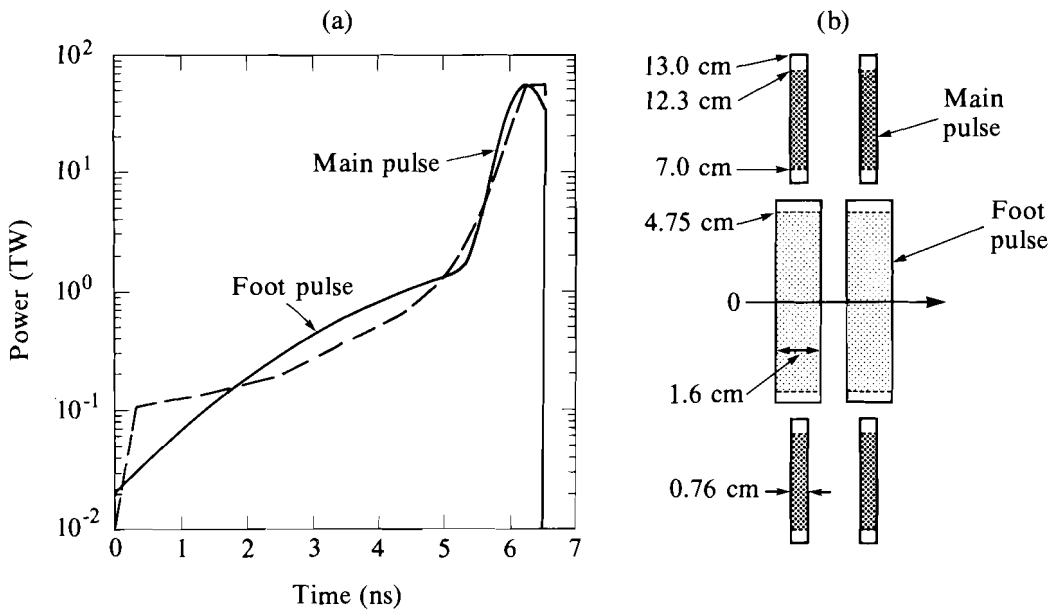

Fig. 39.2
Dual-pulse basis of upgrade design. (a) Double-Gaussian temporal profile of laser power formed by superposing a long foot pulse and a short main pulse, approximating the ideal shaped pulse shown dashed; (b) cross section of co-propagated foot and main beams at the frequency-conversion crystals.

Fig. 39.2(b)]. Each beam is azimuthally symmetric about the propagation direction (shown as an arrow in the figure). Co-propagation begins at the front end of the laser, where two oscillator pulses are first amplified in separate driver lines, and then appropriately apodized and combined into a single beam, which is maintained through the remainder of the laser system. At the end of the infrared portion of the system, conversion crystals of two different thicknesses are mounted one inside the other, each crystal optimized for the beam incident upon it. The beam dimensions at the crystals are chosen so that the UV energy loading, multiplied by a safety factor to accommodate UV hot spots, does not exceed the damage threshold of the high-reflectance and anti-reflection coatings following the crystals.

The shaded areas in Fig. 39.2(b) represent nominal beam areas and the solid edges indicate the clear aperture. Beam energy will actually spread a little outside the shaded areas, but the main and foot beams will remain distinct. The IR beam emerging from the last amplifier is expanded to accommodate the lower UV damage thresholds. Figure 39.2(b) is schematic; the method by which the crystals are mounted is not discussed here. The use of two separate crystals has been found to be more cost effective than the single "top-hat" crystals proposed in Ref. 5.

One other advantage of propagating the foot pulse through just a portion of the whole aperture is that while the total power ratio is ~20:1, the intensity ratio on the crystals is only 5:1, allowing for thinner foot-pulse crystals than would otherwise have been called for. It is important to note that this co-propagation configuration only works because we are using distributed phase plates (DPP's)[6,7] at the focusing lenses; since each DPP element irradiates the whole target, the locations of the foot and main beams in the near field are immaterial. Without DPP's, the target would be irradiated with annular main beams, which would be unacceptable from the point of view of uniformity. DPP's are also essential components for SSD, a technique for obtaining good irradiation uniformity on target that has been developed at LLE[8] and forms an integral part of the upgrade design.

Performance Parameters

Parameters anticipated for the main and foot pulses are listed in Table 39.I, for a main-pulse width ranging from 0.5 to 0.75 ns and a foot-pulse width from 3 to 5 ns. They are derived by working back from the energy and pulse shape needed at the target. The design of the upgrade is based on a requirement that 24 kJ of UV main-pulse energy be available on target in the front 80% of a Gaussian whose full width can vary in the range 0.5 ns–0.75 ns, with 6 kJ of foot-pulse energy in the front half of a Gaussian of full width 5 ns. Using a measured DPP efficiency of 79% (into the central disk of the focal spot) and assuming a 9% transport loss (including a 4% diagnostic pickoff and 0.5% from each coated surface), one can calculate the UV energy required from each crystal. Knowing the (intensity-dependent) pulse shortening produced in the crystals, one can then work back to find the IR energies and pulse widths required at the crystal input. Numerical modeling of all portions of the system is used to calculate

Table 39.I Anticipated performance of OMEGA Upgrade

	Main Pulse		Foot Pulse	
Beam area (cm^2)	321		71	
Temporal shape	Gaussian		Half-Gaussian	
Crystal thickness L (cm)	0.76		1.6	
UV FWHM (ns)	0.50	0.75	3.0	5.0
IR FWHM (ns)	0.56	0.9	3.3	5.56
Nominal IR intensity on crystal I_0 (GW/cm^2)	5.47	3.38	0.98	0.98
Normalized IR intensity of most intense ray[(a)]	5.14	3.18	4.08	4.08
Operating point of most intense ray[(b)]	M_1	M_2	F	F
Frequency conversion efficiency (%)	80	70	75	75
IR energy per beam on to crystals (J)	977	977	116	194
UV energy per beam out of crystals (J)	782	684	87	146
UV energy per beam on target (J)[(c)]	564	493	62.7	105
Average UV energy loading after crystals (J/cm^2)	2.4	2.1	1.2	2.1
AR damage fluence for full Gaussian (J/cm^2)	3.8			6.8
Peak UV power on target (TW)	63.5	37.1	2.4	2.4
Total UV energy on target (kJ)	33.8	29.6	3.8	6.3
Truncated UV energy on target (kJ)[(d)]	27.1	23.7	3.8	6.3

[(a)] $0.9394\ I_0(L/0.76)^2$. See Fig. 39.3

[(b)] See Fig. 39.3

[(c)] Assumes a 9% transport loss and a DPP efficiency of 79% (into the central disk of the focal spot)

[(d)] With truncation of the last 20% of the main-pulse UV energy

TC2631

the pulse shapes and other parameters at the oscillators required to give the desired pulse shape on target.

The foot pulse is truncated at its peak to reduce the energy loading on coatings, as the second half of the foot-pulse Gaussian is obviously irrelevant to the target implosion; however, since the damage fluences associated with truncated laser pulses have not yet been measured, the system is designed conservatively so that it will not damage at the fluences that would result if the electro-optic device that truncates the pulse were to fail. The weakest anti-reflection coating in the UV subsystem is the sol-gel coating on the final KDP surface; its damage threshold for full Gaussian (i.e., untruncated) pulses varies from 3.8 to 6.8 J/cm^2 for pulse widths of 0.5 to 5 ns. The coating will handle the anticipated UV energy loadings at both pulse widths, even if the foot pulse is not truncated, with a safety factor of 1.6:1–1.8:1 to accommodate UV hot spots (i.e., modulations of the near-field UV intensity distribution that might arise from diffraction in the system). It is also planned to truncate the last 20% of the main-pulse Gaussian, which also is of little value to the implosion. Again, the system is

designed conservatively so that it will handle a non-truncated Gaussian main pulse, although under routine operating conditions the last 20% of the UV energy will be truncated.

Table 39.I gives the parameters associated with a Gaussian main pulse; this is also convenient because the intensity, pulse width (FWHM), area, and energy are then related in the obvious way. The actual, truncated energies that will be obtained on target are given in the bottom line. The total energy available will depend on the combination of main- and foot-pulse widths selected; however, it is evident that, for the longer foot pulse, a total of 30 kJ of useful on-target energy will be available throughout the range of main-pulse widths.

The parameters given in Table 39.I allow for reasonable flexibility in pulse shaping. Greater flexibility is possible, since pulses as short as 100 ps and as long as 10 ns can be obtained from the main- and foot-pulse oscillators, respectively. However, with pulse widths outside the ranges indicated in the table, less than 30 kJ will be available. For shorter pulses the system is intensity limited, while for longer pulses it is energy limited in the IR and experiences a lower frequency-conversion efficiency. The system is potentially capable of producing an extra 3 kJ in the main pulse at the shorter pulse width of 0.5 ns (27 kJ rather than the 24 kJ required), because higher conversion efficiencies are obtained at higher input intensities, but this will only be possible if the UV coatings can handle the extra loading (2.4 rather than 2.1 J/cm^2).

The characteristics of the frequency-conversion crystals are shown in Fig. 39.3, for rays of a single intensity I. By using the intensity normalized to the thickness of the main-pulse crystals on the abscissa $I' = I(L/0.76\text{ cm})^2$ where L is the crystal thickness, the same curve can be applied to both the main pulse and the foot pulse to a good approximation. (The calculation is exact for $L = 0.76$ cm; about 3% lower efficiencies are actually obtained for the foot pulse due to greater IR absorption in the thicker crystals.) The operating points corresponding to the intensities found at the peaks of the pulses are indicated for the 0.5-ns and 0.75-ns main-pulse options (M_1 and M_2, respectively), and for the foot pulse (F, independent of pulse width). Larger overall efficiencies than 82.5% could be obtained for the integral over a Gaussian temporal shape for the 0.5-ns main pulse by operating to the right of M_1, but we prefer to avoid this regime because of an increased sensitivity to depolarization in the beam. The point M_2 for the longer 0.75-ns main pulse lies to the left because we are assuming an unchanged infrared energy out of the amplifiers; M_1 is approximately the current operating point on OMEGA. The foot pulse would also operate at M_1 with a choice of 1.8-cm-thick crystals; however, we plan to save costs by using existing 1.6-cm-thick OMEGA crystals, each of which can be cut in half and reworked, and operating instead at point F with $\approx 5\%$ lower conversion efficiency. (The figure of 74.7% quoted for the integration over a Gaussian takes IR absorption fully into account.) It is also worth noting that it is undesirable to design the crystals with the operating point of the

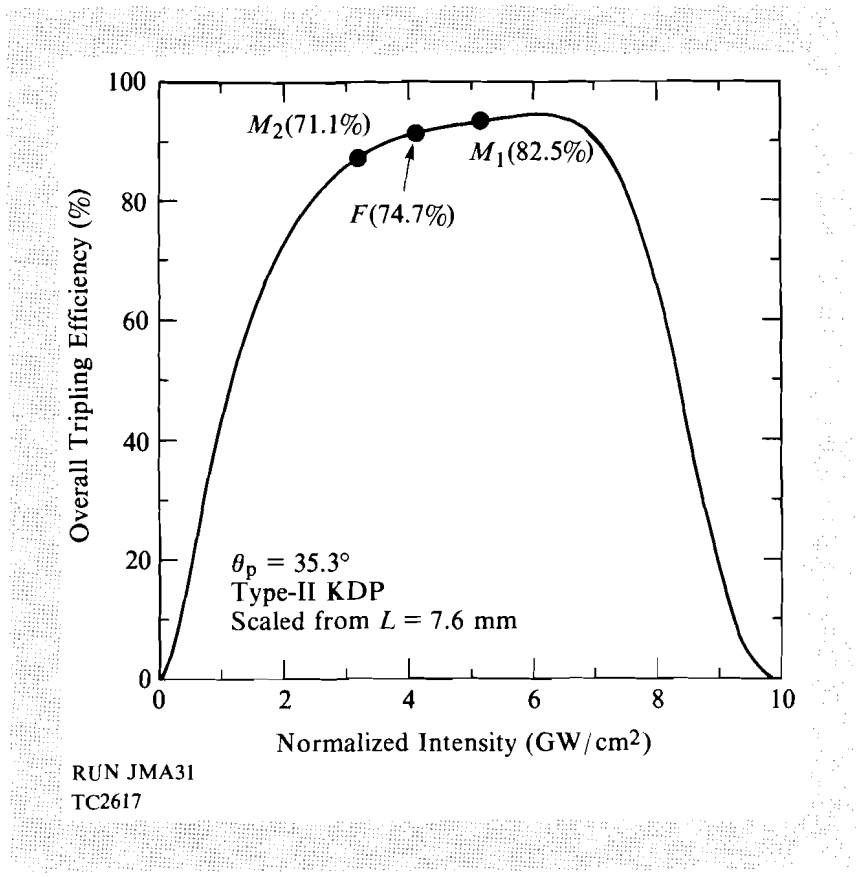

Fig. 39.3
Ideal third-harmonic generation efficiency for a single ray as a function of normalized intensity I' [= $I(L/0.76)^2$ where L is the crystal thickness in centimeters]. M_1, M_2, and F indicate operating points for the main pulse (0.5 and 0.75 ns) and for the foot pulse. Corresponding averages over a temporal Gaussian (or equivalently a half-Gaussian) are shown in parentheses.

system at maximum energy too far to the left in Fig. 39.3, because the falloff of conversion efficiency at high intensity serves to protect the system against the formation of near-field UV hot spots from near-field IR hot spots.

Overall Layout of Upgrade

The overall layout planned for the upgrade is illustrated in Figs. 39.4 and 39.5. The need to fit all the hardware (including the extra amplifiers, the extra beamlines, and a larger target chamber) into existing building space has led to a substantial rearrangement. The oscillators and driver lines, including SSD hardware and the means to combine the two beams into a single co-propagated beam, will be located in the capacitor bays beneath the floor of the existing laser bay. The co-propagated beam will be transported to the laser bay and split into 15 beams in two stages, a three-way split followed by a five-way split, with an existing OMEGA 64-mm rod amplifier following each split (amplifier stages A and B of Fig. 39.5). All beam splitters will have motorized, automated polarization control to provide for accurate energy balance. The 15 beams will be propagated through existing 90-mm OMEGA amplifiers (stage C) and spatial filters in the center of the bay in three stacks of five each. Each beam is split four ways at the end of the bay, at which point the 60 resulting beams pass through assemblies that permit ± 1.5 m of gross path-length adjustment needed to compensate for the inequality in transport paths to the target chamber and to provide precision beam-timing capability.

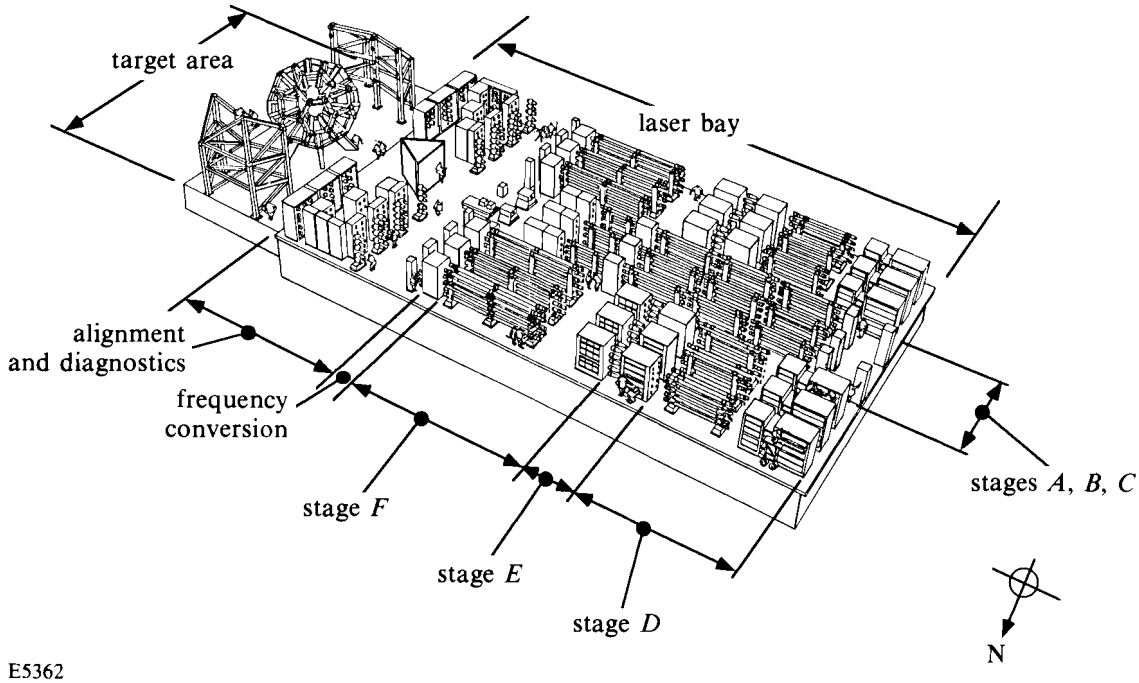

Fig. 39.4
Perspective view of the OMEGA Upgrade.

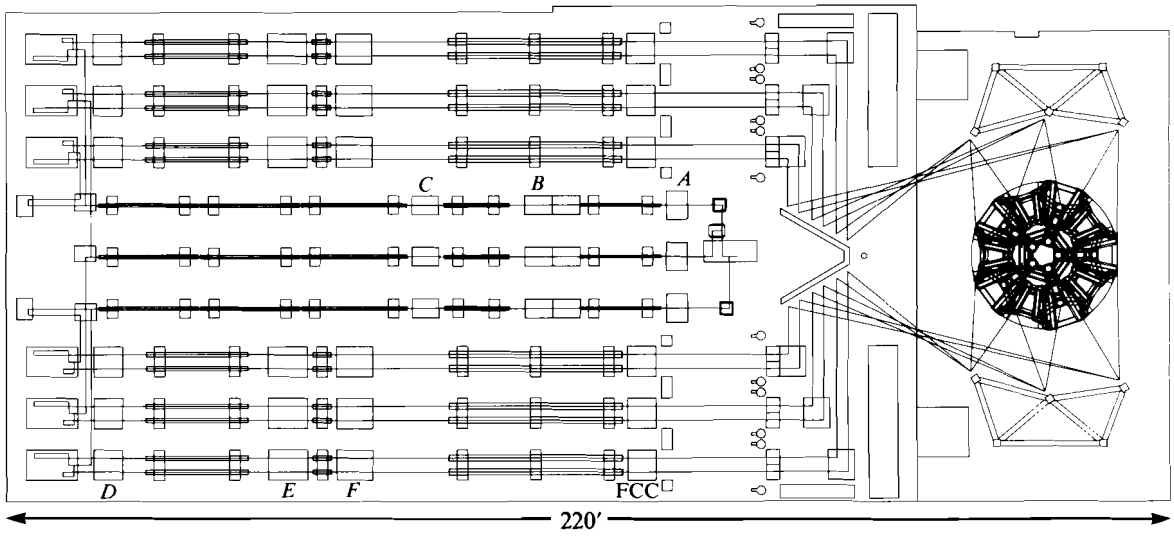

Fig. 39.5
Layout of the OMEGA Upgrade. The location of four stages of rod amplifiers (*A-D*), two stages of disk amplifiers (*E,F*) and the frequency-conversion crystals (FCC's) are indicated.

The 60 beams then propagate back near the outside of the bay in six clusters of ten beams (two wide, five high); each beam will pass through another 90-mm rod amplifier (stage *D*), through two stages of disk amplifiers (*E* and *F*), and onto the frequency-conversion crystals (FCC's). Thin-film polarizers will be used immediately prior to the crystals to ensure that the correct linear polarization is incident upon the crystals. After frequency conversion, a small fraction of the energy of each beam will be split off for energy diagnostics at the fundamental, second harmonic, and third harmonic, with separate measurements for the foot and main pulses; the UV beams will then be transported to the target chamber, half approaching from each side rather than all directly from the V-shaped structure as presently configured.

At each stage, spatial filtering will be used to remove high-spatial-frequency noise from the beam and to ensure correct image relaying.[9] Image relaying is also important for SSD, to prevent different frequencies from wandering excessively across the beam cross section due to the grating-induced differences in their propagation directions, and to prevent the formation of intensity modulations through interference effects. In particular, the annular dead zone at the co-propagation apodized aperture (between the main and foot beams) must be imaged to the dead zone between the crystals. The size of the dead space or "anti-mix" zone between the foot and main pulses is chosen to be sufficient to prevent spatial overlap of the two pulses, but is otherwise minimized to save on the aperture of disks and other optical components.

The IR portion of the system is analyzed in detail using two codes: RAINBOW, a ray-tracing code, which includes experimentally measured amplifier gain profiles and gain saturation,[10,11] and MALAPROP,[12-14] which models diffraction and nonlinear effects (including amplitude and phase noise) in various optics and spatial filters. Given the beam parameters required at the input to the frequency-conversion crystals, we can iteratively calculate the IR parameters required at the input to the driver line.

Oscillators and Driver Lines

The foot pulse will be generated in a self-seeded, single-mode, Nd:YLF Q-switched oscillator. The monomode character of the emission of this oscillator is guaranteed through intracavity etalons and an extended low-level prelase phase. The oscillator will emit 10- to 20-ns pulses from which 3- to 6-ns shaped pulses will be carved out. For the main pulse the output of a cw mode-locked master oscillator will be used to seed a regenerative amplifier. Flexibility of adjustment of the pulse width from 500 to 900 ps will be provided by the insertion of intracavity etalons into the cw master oscillator. The central wavelengths of the two oscillators will be stable to 0.1 Å, which will ensure less than 1% degradation of the third-harmonic conversion efficiency.

The synchronization of the main and foot pulses will be achieved through a combination of (a) synchronized Q-switches for the main-

pulse and foot-pulse generators; (b) two rf-synchronized, cw mode-locked, master oscillators seeding two regenerative amplifiers for the main pulse and an auxiliary short-pulse switching laser; (c) a pulse generator with a ps-precision delay; and (d) optoelectronically triggered high-voltage pulse generators. These latter pulse generators drive Pockels cells that are used to shape the foot pulse as well as to truncate the foot and main pulses.[15,16]

There are presently two designs under consideration for the main-pulse and foot-pulse driver lines: one is based on the present OMEGA driver line with only minor modifications; the other is based on a large-aperture, imaging, unstable resonator operating as a regenerative amplifier. Both designs incorporate SSD gratings and an rf phase modulator.[8] The trade-off between the two driver-line designs will be based on the results of experiments on large-aperture regenerative amplifiers, which have recently been initiated. Apodization of the driver lines prior to combination into a single co-propagated beam will be performed using LLE-developed liquid-crystal apodizers.[17,18]

Disk Amplifiers

The disk amplifiers will be of conventional box geometry.[19,20] A 15-cm-diameter stage will be followed by a 20-cm-diameter stage, each containing four disks (see Fig. 39.6). The clear aperture of the final amplifier is set by damage constraints, specifically the sol-gel anti-reflection coating on the input lens to the final spatial filter that damages when the main pulse reaches 9.8 J/cm^2 (of untruncated energy). The 15-cm stage provides a main-pulse saturated gain of 3.1, and the 20-cm stage a gain of 2.3. Saturated gains for the foot pulse will be slightly lower because the longer pulse operates at a higher fluence.

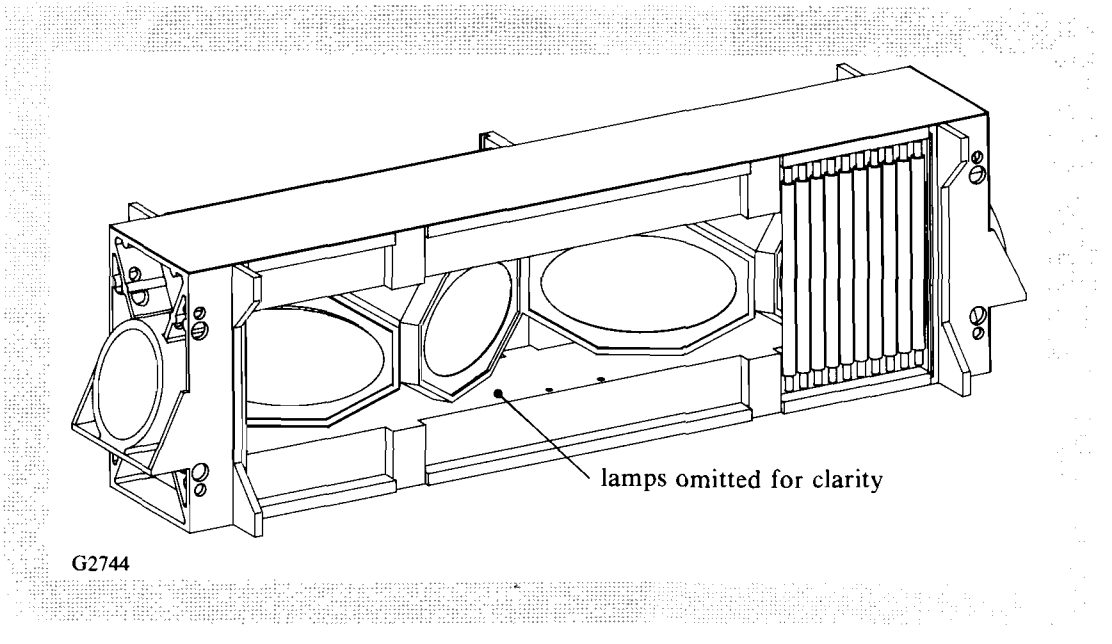

Fig. 39.6
Schematic of a 20-cm-aperture disk amplifier.

Both stages will be able to use the same power-conditioning pulse-forming network. The stages will be separated by a beam expander rather than a spatial filter, and therefore have to be considered as a single stage in calculations of the B-integral. (The B-integral is the phase delay accumulated in a high-power laser beam due to the nonlinear, intensity-dependent refractive index; small values of B are desired in order to minimize the possibility of self-focusing.) The ΔB for the combined stage (pinhole to pinhole) is a modest 1.6 for the main pulse, less than the traditional limit per stage of 2.0.[21] The B-integral is not a consideration for the foot pulse, which operates at a lower intensity than the main pulse. Cooling times for the amplifier disks will be sufficiently short to permit a 1-h shot cycle.

The disk-amplifier design makes use of water-cooled flash lamps in order to operate with a high storage efficiency, for reasons of economy. The modular nature of the design allows for the rapid change of gain medium and/or pump modules within the shot cycle.

In earlier designs for the upgrade we considered using 15 multisegmented amplifiers (MSA's), each amplifying four beams.[5] However, in order to obtain power balance on target,[22] it is necessary to balance the amplifier gain between individual beamlines. The MSA concept, while delivering improved efficiency, did not lend itself to adjustment of individual beamline gains. For this reason, and because of the higher gain offered by single-beam box amplifiers, we have opted for the box amplifier in our current design. We are completing construction of a prototype MSA, which we will test as part of our laser-development program in parallel with upgrade design activity.

Location of Frequency-Conversion Crystals

The frequency-conversion crystals will be placed in the laser bay, after the IR portion of the system but before transport to the target area. Earlier designs for the OMEGA Upgrade considered placement of the crystals on the target structure just after the last reflecting mirror, as on NOVA, except that the crystals would not be placed so close to the focusing lenses. This has the advantages of totally avoiding the need for high-reflectance UV coatings and minimizing the propagation distance of UV radiation, but these are outweighed by a number of drawbacks, some of which are listed here: (a) it is uncertain whether 0.76-cm-thick crystals of ~30-cm aperture can be mounted in all orientations without encountering problems associated with gravitationally induced stress; (b) the target-mirror structure would be crowded by a large number of components; (c) the IR beam could suffer some depolarization as a result of the multiple reflections off transport mirrors; (d) accurate measurement of the main-beam and foot-beam energies and conversion efficiencies would be precluded; (e) there would be a risk of crystals and associated optics being damaged by ghosts from the focusing lenses; and (f) the crystals would not be located near an image relay plane.

All of these drawbacks are avoided by placing the crystals in the laser bay, vertically mounted. The critical factor determining the total energy capability of the system now becomes the damage threshold of

high-reflectance UV coatings. Coatings for which this threshold is 3.0 J/cm^2 at 0.5 ns, for an untruncated UV pulse, have been demonstrated at LLE.[23] With modest technological development it is anticipated that the design goal of 3.8 J/cm^2 will be achieved.

Beam Propagation

The baseline design for the mirror configuration required to transport the UV beams to the target chamber uses the system shown in Fig. 39.5, which is similar to that now used on OMEGA and has the advantages of simplicity and low cost. However, two concerns have been raised that could lead to amendment of this design should either prove to be warranted.

The first concern is the possibility of stimulated rotational Raman scattering (SRRS)[24] associated with the nitrogen in the ~40-m-long air path from the frequency-conversion crystals to the target chamber. For a nondepleted pump-laser beam with time-dependent intensity $I_L(t)$, the intensity I_S of the Stokes wave grows exponentially with propagation distance z as

$$I_S(z, t) = I_{So} \exp[g_R I_L(t) z], \tag{1}$$

where g_R is the steady-state gain coefficient for the SRRS process in air and I_{So} is the optical noise field at $z = 0$. Equation (1) is valid provided that the pulse width τ_L of the pump laser is long in comparison with the response time τ_R of the SRRS process. For short laser pulses ($\tau_L \lesssim 10\ \tau_R$) the scattering is transient, and Eq. (1) is replaced by the following equation[25]:

$$I_S(z, t) = I_{So} \exp\left[2(g_R I_L(t)\ zt/\tau_R)^{1/2} - t/\tau_R\right]. \tag{2}$$

Substantial amplification of the optical noise field must occur before significant scattered light is detectable. For typical conditions, the gain factor G [i.e., the argument of the exponential in Eqs. (1) and (2)] must reach approximately 30–35. We can estimate G by using parameters reported for air[24,26] and extrapolated to our conditions: $g_R = 2.5$ cm/TW at 1054 nm and 7.5 cm/TW at 351 nm, and $\tau_R = 0.133$ ns. Clearly Eq. (1) applies for the foot pulse and Eq. (2) for the main pulse. To obtain worst-case estimates, we use the peak UV intensities I_{Lo} out of the frequency-conversion crystals, obtained from the peak IR intensities at the crystal input assuming a 90% instantaneous tripling efficiency (see Fig. 39.3), and we neglect transport losses due to diagnostic pickoffs. From Table 39.I we find that $I_{Lo} = 4.63$ GW/cm^2 for the 0.5-ns main pulse, and 0.83 GW/cm^2 for the 5-ns foot pulse. Using (t_L/τ_R) in Eq. (2) for (t/τ_R), we obtain the gain factors given in Table 39.II for various path lengths.

These simple estimates indicate that the main pulse may be above threshold for significant SRRS if the path length is greater than 25–30 m. Clearly we do not wish to operate the upgrade under these conditions, because of the deterioration in beam quality and beam-to-beam energy balance that would result. Since the SRRS process depends on the detailed laser pulse shape, the estimates given here

Table 39.II Exponential gain factor for stimulated rotational Raman scattering

Propagation distance (m)	10	20	30	40
Gain factor for foot pulse	6	12	19	25
Gain factor for main pulse	19	29	36	42

TC2632

should be treated with caution. More realistic calculations and experimental investigations are clearly needed. If SRRS should be found to present a problem, one possible remedy would be to incorporate beam tubes for a portion of the ~40-m beam path.

The second concern arises from second-order propagation effects associated with the angularly dispersed beams generated using SSD.[8] The angular dispersion causes the projections of the wave vectors of the different frequency components in the propagation direction to have a small nonlinear frequency dependence. As a result, the relative phases of these components change slowly as the pulse propagates, and, after long distances, significant amplitude modulation can develop. The amplitude modulations are greater at higher modulation frequencies and bandwidths. As an example, Fig. 39.7 shows the temporal pulse shape of an initially Gaussian beam of 600-ps FWHM, modulated at 10 GHz with a bandwidth of 3 Å (the baseline SSD parameters for the upgrade), after propagation through 40 m with an angular dispersion of 50 μrad/Å. These parameters are representative of typical operating conditions for the upgrade. Considerable structure is seen in the temporal pulse shape. This modulated pulse shape would not be "seen" by the target, as the times at which intensity maxima occur vary across the beam cross section, and each point on the target sees the intensity integrated over the beam cross section because of the spatial averaging afforded by the DPP's; however, these modulations have the potential for damaging optical components and coatings and are best avoided. Whether or not actual damage will occur as a result of these modulations is by no means certain, since the time-integrated energy loading is unaffected. In addition, a margin of error is built into the baseline design that allows for 1.8:1 modulations in the UV energy loading.

This propagation effect must be considered throughout the system. It is minimized in the IR portion, since the grating plane is image relayed through the system and up to the frequency-conversion crystals. At each image plane of the grating the phase relationships of the various frequency components are restored to their initial values, and the purely phase-modulated character of the pulse is recovered. However, significant intensity modulations can develop at intermediate points between relay planes, and the design of the optical layout must ensure that these modulations do not lead to damage. It is especially important to minimize intensity modulations at the amplifiers and frequency-conversion crystals by locating these components near relay planes,

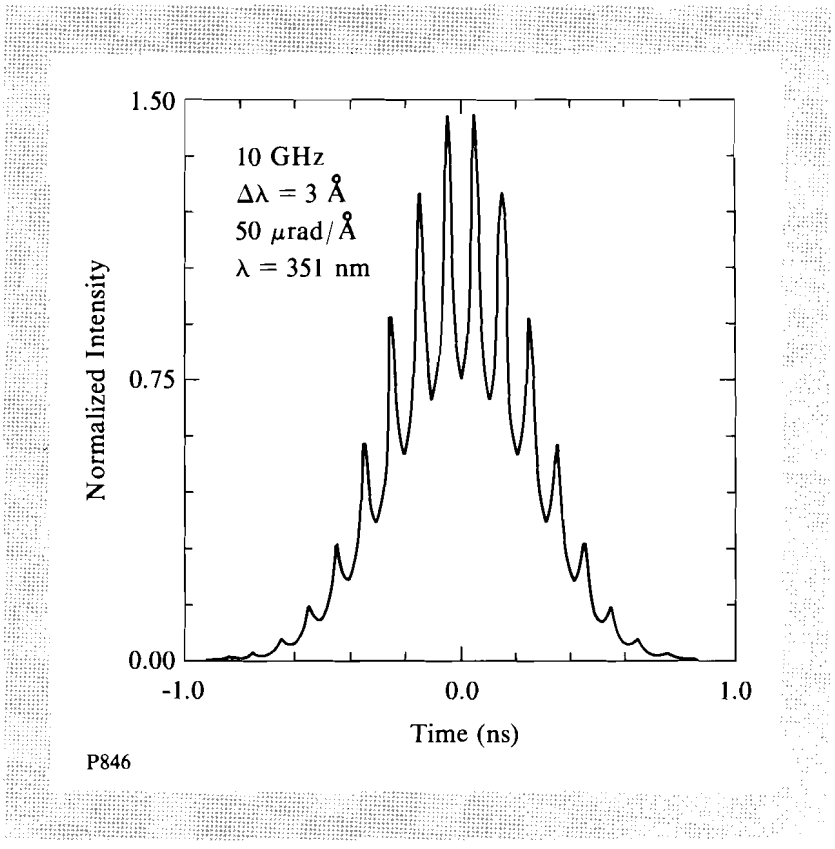

Fig. 39.7
Normalized intensity as a function of time at a point in the cross section of a beam modulated at 10 GHz with a bandwidth of 3 Å, with an angular dispersion of 50 μrad/Å, after propagation through 40 m.

since high intensities increase the risk of self-focusing in laser glass and also lead to reduced frequency-conversion efficiencies. Calculations similar to that of Fig. 39.7 are needed at each stage in the system.

Should the intensity modulations associated with the propagation of UV radiation to the target chamber lead to damage problems, an obvious solution would be to image-relay the UV beam through this path. By doing so, the potential SRRS problem would also be avoided, as a substantial portion of the beam propagation would be through evacuated tubes. While the need for this alternative has not yet been established, it has the merit that possible problems associated with both SRRS and SSD beam propagation would be simultaneously overcome. Detailed calculations and propagation experiments are planned to clarify this issue.

Target Area

The target-mirror structure (see Fig. 39.8) will be highly modular, with five-fold rotational symmetry about the vertical axis reflecting the soccer-ball symmetry in the beam placements. The design provides for segmented platforms and integrates the optical mounts with structurally rigid hexagonal beam tubes. The target mirrors are mounted in boxes on the ends of the beam tubes, which may also serve to provide an isothermal environment for optical components. The beam-transport geometry is such that no angle of incidence at a target mirror will exceed 60°.

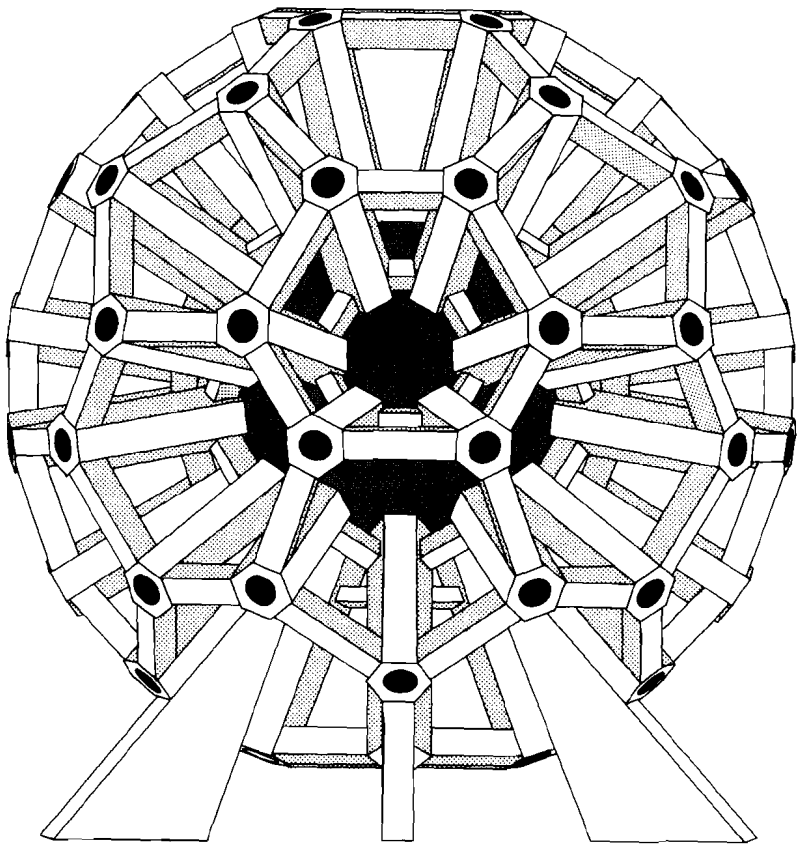

Fig. 39.8
Target-mirror structure for the OMEGA Upgrade.

The target chamber will be 1.8 m in radius and will be constructed out of aluminum alloy, aircraft titanium, or stainless steel. It will also make full use of the soccer-ball geometry. In addition to the 60 beam ports (of diameter 30 cm), there will be 32 diagnostic ports, 20 of large diameter (60 cm) on the hexagonal faces and 12 of smaller diameter (45 cm) on the pentagonal faces. The large diagnostic ports will be particularly useful for instruments requiring a large solid angle, such as a high-resolution neutron time-of-flight spectrometer. Alternatively, they may be fitted with a reducing flange to allow for the use of existing OMEGA instruments. The present complement of OMEGA diagnostics (with modifications where appropriate) will be available for the upgrade. The upgrade target-area design will actually allow a greater free volume for the placement of diagnostic instruments than is presently the case on OMEGA, because beams are transported to the target-mirror structure from the outside, rather than between the target mirrors and the target chamber.

The high neutron yields anticipated for the upgrade have led us to consider what additional shielding of the target area may be necessary. We have undertaken an extensive joint study with Grumman Aerospace to model the potential adverse effects of neutrons on the target chamber, the target bay, and surrounding areas. We have modeled prompt radioactivity in both silicon semiconductor devices and biological tissue, and the build-up of nuclear activation for a typical target-shot schedule. We have included interactions with the experimental target chamber, the turning-mirror structures, optics, electronics, optoelectronics, building walls, and associated structures, and we have investigated a variety of path configurations for neutron transport.

As a result of this study, additional shielding will be required, and some operating procedures will be revised to limit potential radiation exposure to personnel. For example, the area directly underneath the target chamber, which presently houses the experimental control area, will be remotely operated during a DT-filled target shot, and a "cool down" period between a high-yield implosion and personnel re-entry into the target bay may be necessary. Radiation-monitoring detectors connected to computer-controlled interlocks will be installed in order to eliminate the possibility of inadvertent entry of personnel during cool-down periods and to maximize personnel safety. This study is described in more detail in the following article.

Transverse Stimulated Brillouin Scattering

Transverse stimulated Brillouin scattering (TSBS) has been observed in many laser systems.[27–29] It involves the generation of an acoustic wave that propagates in a direction perpendicular to the direction of the incident laser within an optical material. TSBS must be avoided as acoustic intensities can be large enough to fracture an optical element. We have investigated this process and found that it is not a concern for the OMEGA Upgrade.

The equations for TSBS are similar in form to the equations describing SRRS [Eqs. (1) and (2)], with the Raman gain and response time, g_R and τ_R, replaced by the Brillouin gain and response time, g_B and τ_B, and with z replaced by an interaction length within an optic transverse to the laser propagation direction. Generation of TSBS is most likely to occur in the fused-silica substrates near the target chamber. We estimate the gain factor G using parameters reported for fused silica[28,29]: g_B = 4.48 cm/GW at 488 nm, and τ_B = 1.0 ns. For z in the main beam we use 21 cm, the length of the largest chord within the annulus $[2(R_2^2 - R_2^1)^{1/2}$ where R_2 and R_1 are the outer and inner radii, approximately equal to 12 cm and 6 cm, respectively, from Fig. 39.2]. For the foot pulse, z = 9.5 cm from Fig. 39.2. Again we use intensities 4.63 GW/cm^2 for the 0.5-ns main pulse and 0.83 GW/cm^2 for the 5-ns foot pulse.

Here, the transient formula [Eq. (2)] gives G = 29.0 for the main pulse. For the foot pulse, the process is intermediate between the transient and steady-state regimes, which give G = 21.6 and 35.3, respectively. (Note that the TSBS response time of 1 ns is much longer

than the SRRS response time.) From these figures and the same criterion that G must reach 30–35, it is unlikely that TSBS will prove to be a problem. In addition, the gain for the TSBS process has been shown to decrease significantly with the introduction of just a small amount of bandwidth (a fraction of an angstrom in the IR) onto the laser,[29] substantially less than the bandwidth we plan to use with SSD. TSBS is therefore not a concern for the OMEGA Upgrade.

Alignment

The upgrade alignment system will use two wavelengths, unlike the current system that is aligned from the oscillator to the target in the IR. While this will increase complexity, it will eliminate the two main disadvantages of single-wavelength alignment: the transport mirrors will no longer need dual IR/UV coatings, and it will not be necessary to translate the focus lenses through ~109 mm after IR alignment to compensate for their chromatic shift. The IR portion of the laser will be aligned using a 1054-nm YLF laser, together with sensor packages at two locations within each laser chain consisting of a CCD camera, imaging optics, and a shutter to protect the package during a laser shot. The UV portion will be aligned using a 351-nm laser injected through a fiber optic at the UV focus of the IR spatial filter following the last amplifier.

At the heart of the alignment system will be ten mobile full-aperture sensors using all-reflecting achromatic optics, arranged in two stacks of five each, one stack for each side of the laser bay. The sensors will view small fractions of the IR beam energies transmitted through the first mirrors past the frequency-conversion crystals (the "end mirrors"). Each stack will be moved sequentially to six locations to accomplish IR beamline alignment and IR-to-UV alignment. Finally, target alignment will be done by moving the sensors to a seventh location where they will view UV reflections from a surrogate target transmitted back through the end mirrors and reflected by a roving fold mirror, again five beamlines at a time corresponding to six locations of the fold mirror.

Laser Diagnostics and Control Systems

The laser-alignment, diagnostic, and power-conditioning subsystems all rely heavily on computer control and data-acquisition systems. On the current OMEGA laser these systems are largely independent; for the upgrade, developments in network technology will be used to facilitate high-speed communication among the different systems.

Beam-energy measurements are required at various points in the laser chain. The most important measurement is made just after the frequency-conversion crystals, where a Fresnel-reflection pickoff from an uncoated surface is used to transport 4% of the beam energy into a diagnostic package. This is similar to the multiwavelength energy-sensing system (MESS) currently used on OMEGA, except that two integrating spheres will be used, one for the main pulse and one for the foot pulse. The optical layout will ensure that the co-propagated aperture is relayed to the rear surface of the first (main-pulse) integrating sphere, so that the foot pulse will pass through to the

second integrating sphere. Separate measurements will therefore be possible for the main and foot pulses at all three wavelengths (1054 nm, 527 nm, and 351 nm).

In order to ascertain the UV energies actually incident on target, accurate measurements of the transport losses from the pickoff to the target are required for each beam line. At present, these losses are measured by a small positionable integrating sphere, which is inserted into the center of the target chamber and successively pointed in each of the 24 beam directions. A similar system will be used for the upgrade.

Summary

We have presented an overall description of the preliminary design for the OMEGA Upgrade. This design is based on existing technology and available optical materials; in addition, it has the potential to benefit from a number of new developments and extensions of existing technology that are anticipated to mature in the near future. We have identified areas where further studies and prototyping are necessary before arriving at the final design. We are aware of no reason why the upgrade should not be able to provide the additional laser energy, uniformity, flexibility, and pulse-shaping capabilities required for future research in direct-drive laser fusion on the OMEGA system.

ACKNOWLEDGMENT

This work was supported by the U.S. Department of Energy Office of Inertial Fusion under agreement No. DE-FC03-85DP40200 and by the Laser Fusion Feasibility Project at the Laboratory for Laser Energetics, which has the following sponsors: Empire State Electric Energy Research Corporation, New York State Energy Research and Development Authority, Ontario Hydro, and the University of Rochester. Such support does not imply endorsement of the content by any of the above parties.

REFERENCES

1. *New Scientist*, 31 March 1988, p. 36.
2. C. Vaughan, *Science News* **135**, 56 (1989).
3. D. Eimerl, *IEEE J. Quantum Electron.* **QE-23**, 1361 (1987).
4. R. S. Craxton, *IEEE J. Quantum Electron.* **QE-17**, 1771 (1981).
5. LLE Review **38**, 79 (1989).
6. Y. Kato *et al.*, *Phys. Rev. Lett.* **53**, 1057 (1984).
7. LLE Review **33**, 1 (1987).
8. S. Skupsky, R. W. Short, T. Kessler, R. S. Craxton, S. Letzring, and J. M. Soures, to be published in *J. Appl. Phys.* See also LLE Review **37**, 29 (1988); LLE Review **37**, 40 (1988).
9. J. T. Hunt, P. A. Renard, and W. W. Simmons, *Appl. Opt.* **16**, 779 (1977).
10. L. M. Frantz and J. S. Nodvik, *J. Appl. Phys.* **34**, 2346 (1963).

11. W. E. Martin and D. Milam, *IEEE J. Quantum Electron.* **QE-18**, 1155 (1982).

12. W. W. Simmons, J. T. Hunt, and W. E. Warren, *IEEE J. Quantum Electron.* **QE-17**, 1727 (1981).

13. W. W. Simmons and W. E. Warren, presented at *SPIE Technical Symposium on Applications of Artificial Intelligence*, Orlando, Florida, 31 March 1986. Available as Lawrence Livermore National Laboratory Report UCRL 94380.

14. We are indebted to J. Lawson of LLNL for the availability of this code.

15. P. LeFur and D. H. Auston, *Appl. Phys. Lett.* **28**, 21 (1976).

16. G. Mourou and W. Knox, *Appl. Phys. Lett.* **35**, 492 (1979).

17. S. D. Jacobs, K. A. Cerqua, K. L. Marshall, A. Schmid, M. J. Guardalben, and K. J. Skerrett, *J. Opt. Soc. Am. B* **5**, 1962 (1988).

18. J. C. Lee, S. D. Jacobs, T. J. Kessler, and N. Van Lieu, *Technical Digest-CLEO '89*, Baltimore, MD, 1989.

19. M. J. Lubin, J. M. Soures, and L. M. Goldman, *J. Appl. Phys.* **44**, 347 (1973).

20. Laser Program Annual Report–1977, Lawrence Livermore Laboratory, Livermore CA, UCRL 50021-77 (1978), pp. 2-142 to 2-145.

21. J. Hunt *et al.*, UCID-19086, p. 10 (1981).

22. LLE Review **37**, 16 (1988).

23. D. Smith and A. Schmid, unpublished data.

24. M. A. Henesian, C. D. Swift, and J. R. Murray, *Opt. Lett.* **10**, 565 (1985).

25. W. Kaiser and M. Maier, in *Laser Handbook*, Vol. 2, edited by F. T. Arecchi and E. O. Shulz-Dubois, (N. Holland Publ. Co., Amsterdam, 1972), p. 1077.

26. V. S. Averbakh, A. I. Makarov, and V. I. Talanov, *Sov. J. Quantum Electron.* **8**, 472 (1978).

27. J. L. Emmett and L. Schalow, *Phys. Rev. Lett.* **170**, 358 (1968).

28. J. M. Eggleston and M. J. Kushner, *Opt. Lett.* **12**, 410 (1987).

29. J. R. Murray *et al.*, Laser Program Annual Report–1989, Lawrence Livermore National Laboratory, Livermore, CA, UCRL 99914.

1.B Target Experimental System

The target experimental system of the OMEGA Upgrade provides the main facility for performing target experiments, and for acquiring and recording the experimental results. It comprises the following subsystems: the experimental target chamber, the vacuum system, target-positioning systems (for both cryogenic and conventional targets), diagnostic instrumentation, radiation shielding, instrument control and interfacing systems, and the diagnostic control room. In this article, the design considerations for these subsystems are described in detail.

The successful operation of the current OMEGA target experimental facility for the past decade has established a large base of experimental expertise at LLE; this is directly transferable to the OMEGA Upgrade. A new concern is the potential radiological hazards associated with the expected increase in neutron flux. A study has been carried out to address this issue; as a result of this study, additional shielding will be required, and some operating procedures will be revised in order to limit potential radiation exposure to personnel.

Experimental Target Chamber

The design of the experimental target chamber addresses the tasks of target delivery and positioning, stable mounting of the laser-focusing optics, tank pump-down, and containment of radioactive blowoff and target debris. The target chamber will have 60 entrance ports for the laser beams (of 30-cm clear aperture), as well as 20 large-diameter (60 cm) and 12 smaller-diameter (45 cm) ports for diagnostic instrumentation. All of these ports are shown in Fig. 39.9, using a sinusoidal projection. Accurate target positioning in the center of the chamber requires high stiffness and thermomechanical stability of the chamber structure. Precise laser-beam pointing by the chamber-mounted optical assemblies requires better than 10-μrad pointing stability, which equates to differential chamber deflections of less than 50 μm under vacuum and instrumentation loading. Additional constraints result from the activation of the target-chamber materials by thermonuclear neutrons and from the possible ablation of the target-chamber surface, thus restricting the choice for the chamber materials.

Several design and fabrication approaches have been compared in terms of cost, performance, nuclear activation, and ease of manufacturing. The acceptable materials from the standpoint of nuclear activation are aluminum 5083, aircraft titanium, possibly 400-series stainless steel, Kevlar®, and other composites. Some of the design trade-offs are given in Table 39.III.

Eastman Kodak has modeled the deflections of the target chamber under vacuum and diagnostic loading using the finite-element code NASTRAN. The modeling of the chamber used a 1/120th section of the chamber that includes three of the chamber ports. Only vacuum

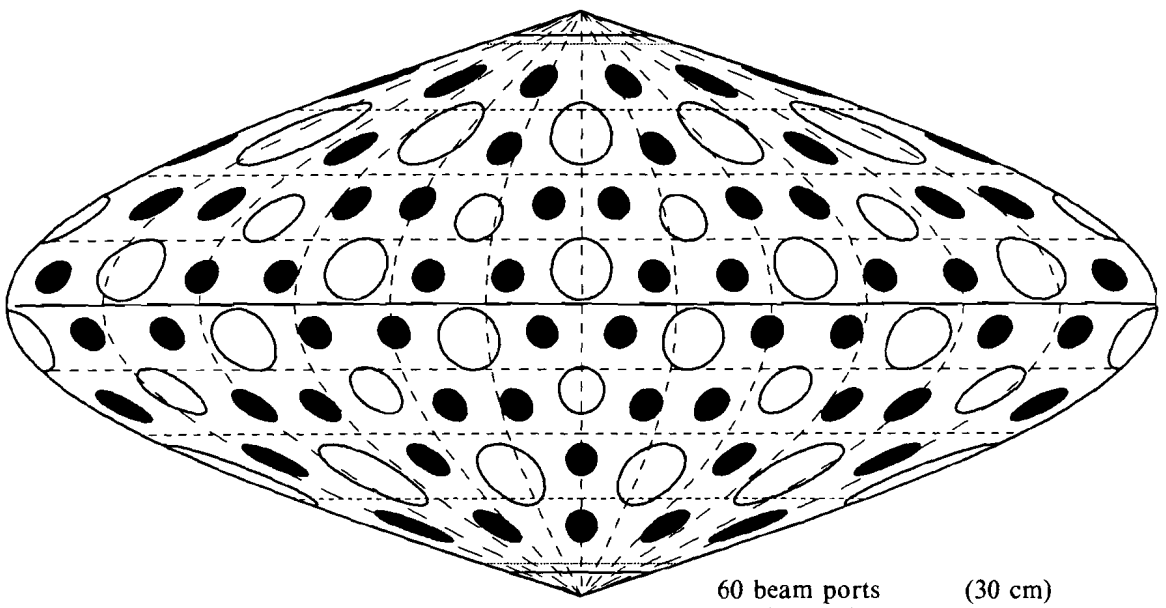

Fig. 39.9
Sinusoidal projection of beam and diagnostic ports for the OMEGA Upgrade. Beam ports are shown shaded; large and small diagnostic ports are centered on the hexagonal and pentagonal faces, respectively.

(0.1 MPa) loading is applied in this model. The support loads are not included in this model, but since conceivable supports are highly symmetric, they are not expected to significantly alter the total deflections. The results of this analysis for a 10-cm-thick aluminum 6061 alloy chamber are shown in Fig. 39.10. The deflections are within tolerances for pointing and location (10 μrad).

From the above considerations, Kevlar® has been ruled out due to cost and complexity. The leading candidate is presently aluminum 5083, mainly due to its lower fabrication cost. However, if final cost quotes and further research into neutron activation show 400-series stainless steel to be acceptable, the decision will be carefully reviewed with respect to all of the performance trade-offs.

Another problem studied was the ablation of the inner wall of the target chamber, due to material and radiation flux following target shots. Analysis shows that regardless of the wall material, ablation will be insignificant. Figure 39.11 shows the damage threshold of aluminum for soft x rays, for photon energies of up to 100 keV. Here, and in subsequent discussions, the damage threshold is defined to be

Table 39.III Design and fabrication approaches for the OMEGA Upgrade target chamber

Material and Method	Comments
• Ti, 1.5–3″ thick, welded hemispheres, or welded flat plates (triangle/hex/pent)	− more expensive than aluminum or stainless steel
	+ high stiffness, low activation
• Ti, inner/outer skins, internal stiffeners	− complex welding, expensive
• Al, 3–5″ thick, welded hemispheres	+ moderate material/machining cost
	+ can be formed and welded
	+ low neutron activation
	− high-activation weld filler
	− structural and thermal stability in question
• 400 stainless steel ~4″ thick, welded hemispheres	+ can be formed and welded
	+ good machineability
	+ high stiffness, good stability
	− more expensive than aluminum
	− neutron activation (not presently modeled)
	− may be too heavy for *in situ* crane
	− magnetic
• Kevlar® winding composite	+ low neutron activation
	− vacuum compatibility and stiffness in question
	− extremely expensive

E5334

any change in the appearance of the surface that is visible under a high-powered (100X) optical microscope. The damage threshold, as expected, exhibits a minimum near the K edge of aluminum, of about 0.7 J/cm^2. If all the 30 kJ of laser energy were converted into x rays, the flux averaged over the chamber wall would be 0.074 J/cm^2, lower than the damage threshold for aluminum by a factor of 10.

The same energy loading (0.074 J/cm^2) can be used to estimate the potential damage to the chamber wall due to scattered (unabsorbed) UV radiation. Previous experiments on metal surfaces[1] indicate single-shot optical-damage thresholds of 0.4 J/cm^2 for normally fabricated aluminum surfaces, and 0.9 J/cm^2 for stainless-steel alloy 304. The damage threshold for titanium is not known, but is assumed to be in the same range as aluminum and stainless steel. Diagnostic devices inserted in the OMEGA target chamber experiencing similar irradiation fluences have shown insignificant mass ablation. We believe the dominant effect of the scattered laser light on the chamber wall will be the desorption of gases from the surface.

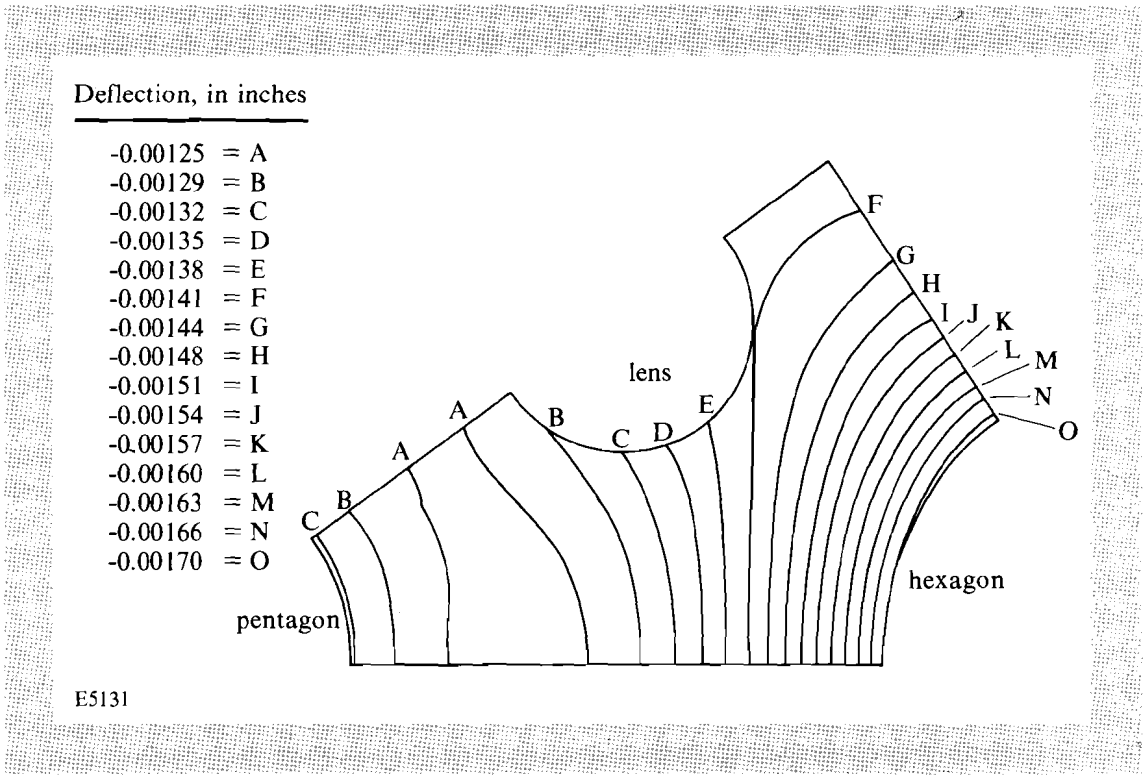

Fig. 39.10
NASTRAN finite-element analysis of a 1/120th section of the upgrade target chamber. Letters denote lines of equal deflection.

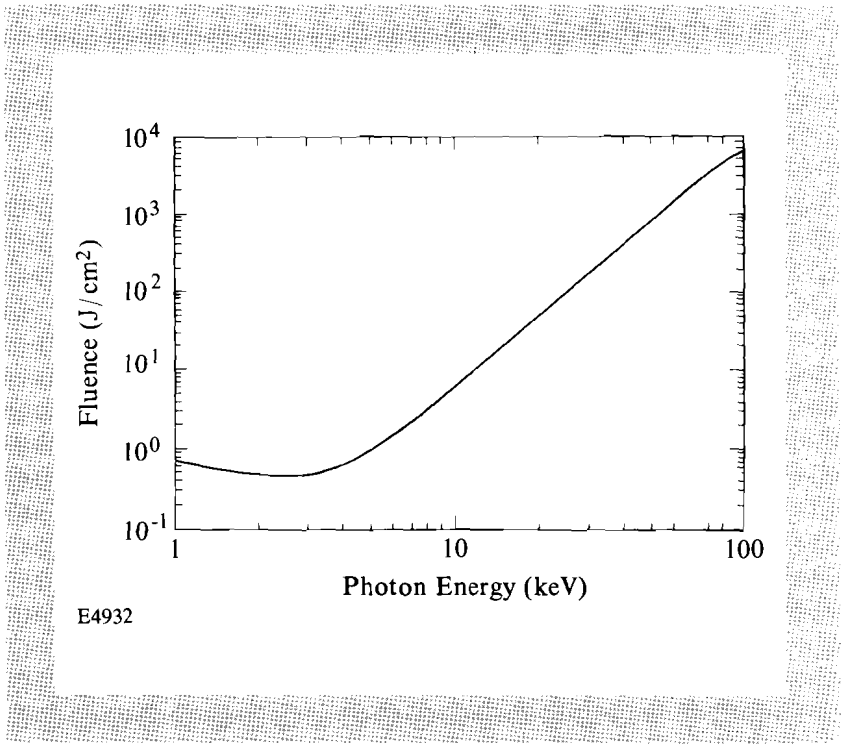

Fig. 39.11
X-ray damage threshold for aluminum subjected to x rays from laser-target interactions in the range 1–100 keV.

In order to estimate the potential effects of high neutron production we use a "maximum-credible neutron yield" derived by assuming that ignition will be achieved. Using Nuckolls' definition of ignition,[2] ignition would imply a gain of ~ 0.3; at $\sim 3.5 \times 10^{14}$ neutrons/kJ, the maximum-credible yield is then 3×10^{15} neutrons. The stresses induced in the target chamber due to this flux and the flux of charged reaction products will be negligible compared with those due to the mounting of diagnostic instruments and vacuum loading. The overpressure at the chamber walls resulting from the deposition of 30 kJ of laser energy in the residual gas of the target chamber (which would be 0.01 MPa or 0.1 atm in a worst-case scenario) may be calculated, following Raizer,[3] to be 1000 Pa. The resulting shock wave causes negligible additional stress in the chamber walls.

The vacuum system for the upgrade experimental chamber is required to have the capability of evacuating the chamber to an ultimate vacuum of 10^{-4} Pa under no load, and to 10^{-2} Pa with the additional vacuum load presented by diagnostic outgassing and helium refrigerant gas used for cryogenic target preparation. The system must contain and dilute (before effusion to the atmosphere) the expected radioactive blow-off from the diagnostic instruments and the tritium gas from imploded DT-fuel targets. Using a large (60-cm diameter) port located on the bottom of the target chamber, a pumping speed of 20,000 liter/s should be obtained; this will be adequate for handling the highest anticipated loading of helium (2 liter/h of He liquid), which is emitted by the cryogenic target-positioning system. With a 20,000 liter/s pumping speed, the system will cycle from atmospheric pressure to operating vacuum in under 2 hours. The vacuum cycling, monitoring, and interlocking will be controlled by a derivative of the current OMEGA vacuum-control system, WATSON. This system has the ability to interlock, monitor, and automatically cycle critical diagnostics depending on the vacuum state, diagnostic requirements, and utility state. We are currently considering conventional diffusion pumps, with nitrogen or freon-refrigerant cold traps, as well as helium-pumping cryogenic pumps. The modest vacuum requirements that apply to laser-target experiments allow vacuum flanges to be sealed with elastomer O-rings.

In the present OMEGA system, the target chamber is pumped to high vacuum at the beginning of an experimental series, and the system is kept at high vacuum for an extended length of time; targets and diagnostic packages are inserted through vacuum locks. This practice reduces motion of the target chamber due to vacuum loading, provides a more consistent vacuum environment for diagnostics, and minimizes problems associated with the release of radioactive waste into the target-bay area. This mode of operation will be continued for the upgrade target experimental chamber.

Target Positioning and Viewing

The target chamber will include a mechanical positioning system to position targets accurately and with repeatability to within 5 μm of the center of the tank. Gas-phase targets will be positioned at the end of a rod of light, low-nuclear-activation material (likely to be a fiber-

composite) by a high-precision 3-axis mechanical positioner located outside the vacuum tank wall.

The cryogenic target-positioning and delivery systems for the OMEGA Upgrade are still under development, but are likely to make use of a combination of techniques employing a retractable cryogenic shroud,[4] jets of cryogenic helium gas, cold-contact fingers, and various target-heating lasers. The system will allow laser implosions of cryogenically prepared glass microballoons, foam shells and spheres, and various light-metal shells. The positioner will have to conform to stringent requirements of positioning and repeatability (5-μm centering tolerance), as well as those of operating in a cryogenic environment. Helium refrigerant will need to be delivered to the target positioner through vacuum-insulated cryogenic transfer lines.

In order to optically locate the target in the experimental chamber prior to laser firing, an accurate high-magnification (100X) target-viewing system will be designed. The viewing system should have two orthogonal lines of sight, and be equipped with digital imaging cameras with video frame-grabbers for documentation and analysis. A low-magnification (10X), wide-angle viewing system will also be provided for coarse positioning of the target and diagnostic instruments. The viewing systems will have the ability to locate and align planar and irregularly shaped targets, in addition to spherical targets. In addition to the main viewing systems, which locate targets at the tank center, an auxiliary target positioner/viewer will be provided to locate targets off-center for x-ray backlighting experiments. Augmenting conventional viewing by imaging or shadowgraphy, target quality will be assessed with interferometers along two axes. These interferometers will allow the evaluation of target quality just prior to implosion for both gas-phase and cryogenically prepared transparent targets. Multiple-wavelength illumination systems for these interferometers will be provided, along with digital image readout with frame-grabbers. The current OMEGA system employs three viewing systems similar to that described above. The interferometers currently in use have dual-wavelength capability and are mounted orthogonally to each other; they can view the formation of the cryogenic fuel layer at times up to a few milliseconds prior to the laser firing.

Diagnostic Instrumentation

The target chamber should provide a rigid and stable platform for accurately mounting and positioning all the currently operative diagnostic instruments. The chamber and mounting structure must not preclude introduction of new or novel diagnostics of any reasonable design. The doubly concentric soccer-ball geometry used for the target chamber and for the mirror-mounting structure allows 20 large-diameter (60 cm) diagnostic ports to be located on the hexagonal faces of the target chamber; these ports have clear access out from the target center to a radius of 6–7 m, all the way to the building walls. This free volume available for placing diagnostic instruments will actually exceed that in the present OMEGA system. These large diagnostic ports will be particularly useful for instruments requiring a large solid

angle (such as a high-resolution time-of-flight neutron spectrometer), or they may be fitted with a reducing flange to allow the use of existing OMEGA instruments (see Fig. 39.12). The 12 smaller (45-cm diameter) ports located within the pentagonal faces of the target chamber have clear access out from the target center to a radius of 4.5 m.

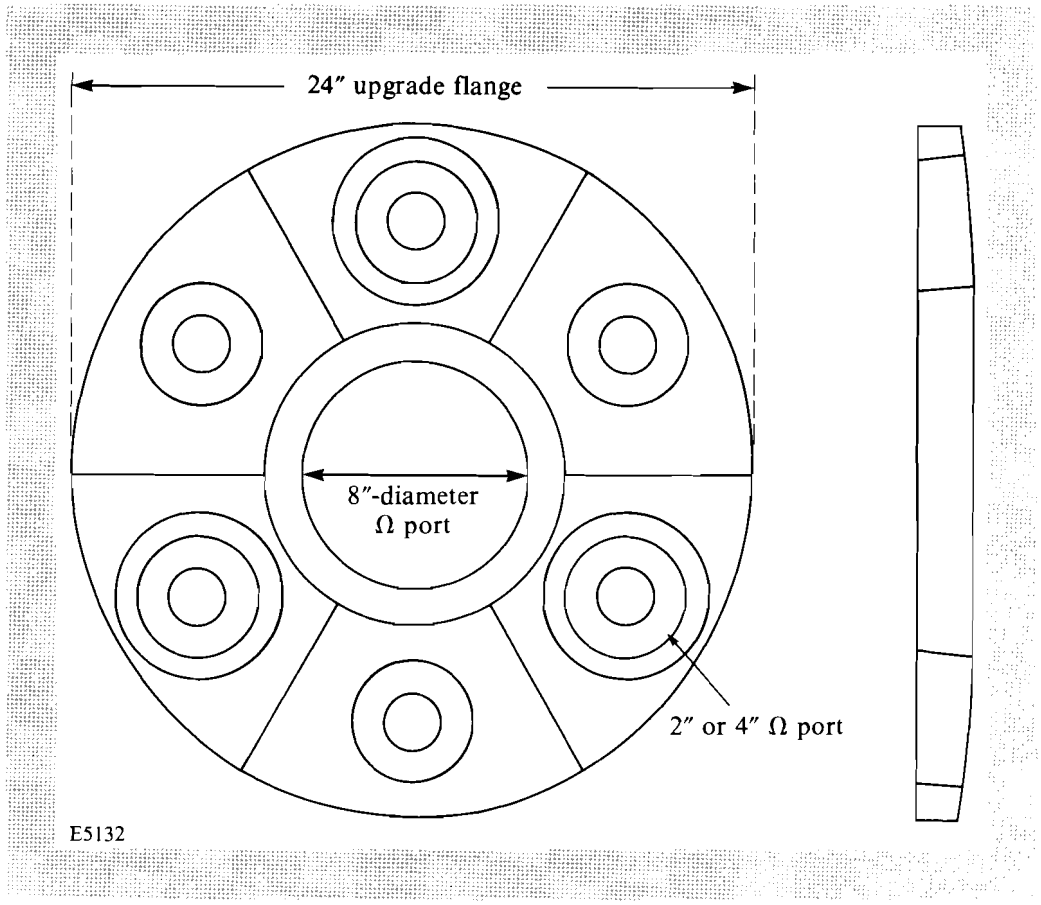

Fig. 39.12
Design of a 24-in. aluminum adapter flange to allow retrofitting of existing OMEGA diagnostic instruments to the upgrade target chamber.

The present complement of nuclear and x-ray diagnostics on OMEGA (see Tables 39.IV and 39.V) will be readily retrofitted to the new chamber, through the use of adapter flanges. Diagnostic devices mounted on the OMEGA Upgrade chamber (of radius 1.8 m) are anticipated to experience x-ray and optical fluences similar to those mounted on the present OMEGA chamber (of radius 0.85 m). The same stringent requirements necessary for the pointing and stability of chamber-mounted final-optic assemblies (0.5-mrad pointing, 50-μrad vacuum deflection) apply to high-magnification imaging diagnostics.

The expected higher neutron yield from the OMEGA Upgrade system permits the use of new neutron-measuring devices, of greatly increased resolution and accuracy. Table 39.IV lists the major nuclear-diagnostic devices, both those existing on OMEGA and those planned

Table 39.IV Nuclear diagnostics for the OMEGA Upgrade

Measured Parameter Currently on OMEGA	Method	Applicability Range
Fuel areal density	Knock-on	Y $\rho R > 3 \times 10^8$ mg/cm^2 $\rho R + \rho\Delta r < 100$ mg/cm^2
Shell areal density	Silicon activation	Y $\rho\Delta r > 1.4 \times 10^8$ mg/cm^2
Fuel ion temperature	Scintillator-PMT	Y $> 7 \times 10^8$ Ti > 1 keV
	array detector†	Y $> 5 \times 10^7$ Ti > 0.5 keV
Primary yield (in DT)	Cu activation	Y $> 1 \times 10^7$
	Na activation	Y $> 5 \times 10^6$
	Ag activation	Y $> 7 \times 10^6$
	Scintillator-PMT	Y $> 5 \times 10^5$
Secondary yield (in DD)	Scintillator-PMT	Y $> 2 \times 10^5$
	array detector	Y $> 2 \times 10^5$
Planned for OMEGA Upgrade:		
Neutron imaging	Penumbral image	Y $> 1 \times 10^{12}$
Neutron emission time	Scintillator-PMT	Y $> 5 \times 10^7$
Neutron "burn" width	n-damaged semiconductor	Y $> 1 \times 10^{12}$
	neutron streak camera	Y $> 1 \times 10^9$

†currently being implemented.

E5321

for the OMEGA Upgrade, and their ranges of applicability. In addition to current diagnostic devices,[5,6] new single-hit, high-resolution neutron-spectrometer prototypes are currently being tested on the OMEGA system;[7] these will provide a baseline for performance evaluation of a larger system to be installed on the OMEGA Upgrade. Cable[8] and Miley[9] have pointed out the benefits of high-resolution primary, secondary, and tertiary neutron spectroscopy as powerful diagnostics for compressed fuel whose applicability will extend to reactor-scale targets. High-accuracy neutron spectroscopy requires a scattering-free environment for the detector, and a clear flight path through an evacuated tube from the target to the detector. Modeling the flight of neutrons and their interaction with the chamber and its

Table 39.V X-ray diagnostic devices implemented on OMEGA

Spectral Diagnostics	
Diagnostic Device	Range of Measurement (resolution)
3-m grazing incidence spectrograph	12–250 Å
1-m grazing incidence spectrograph	25–300 Å
Imaging crystal spectrograph	0.6–25 Å (20 μm)
Time-resolved (streaked) crystal spectrograph	0.6–25 Å (20 ps)
Total Fluence Diagnostics	
Diagnostic Device	Range of Measurement (resolution)
X-ray calorimeters (2)	0–9 keV
Filtered x-ray diodes (4)	0.1–1 keV (150 ps)
Filtered PIN diodes	1.8–5 keV
Filtered NaI scintillators	5–90 keV
Imaging Diagnostics	
Diagnostic Device	Range of Measurement (resolution)
Kirkpatrick-Baez microscopes (2)	2.5 –12 Å (5 μm)
Pinhole cameras (6)	<12 Å (15 μm)
Time-resolved multi-frame cameras (2)	3–12 Å (20 μm; 90 ps)
Time-resolved imaging streak camera	3–12 Å (15 μm; 20 ps)
Spectrally resolved pinhole camera	<12 Å (15 μm; 2.2 Å/mm)

E5322

instrumentation requires Monte-Carlo neutron-transport codes. The distance to the neutron-diagnostic room will be 20–40 m, which will require the construction of a dedicated site outside the target bay (Fig. 39.13). Auxiliary sites along this flight path will be provided for neutron diagnostics at shorter flight paths. With the increase in yields, it should be possible to measure the neutron emission time and neutron "burn" width using techniques developed by groups at Livermore[10–12] and elsewhere.

Characterization of the implosion dynamics of high-convergence OMEGA Upgrade targets and of drive uniformity and symmetry will be carried out using a comprehensive set of x-ray imaging and spectroscopic systems. For the current OMEGA system, time-integrated images with 5-μm resolution, in the wavelength range 2.5–12 Å, are obtained with two Kirkpatrick-Baez microscopes. Six pinhole cameras provide additional coverage below 12 Å, with spatial resolution below 15 μm. One additional multiple-pinhole camera is currently employed in conjunction with an LLNL-developed fast gating system[13–15] that provides several frames with resolution of 90 ps during an interval of ~1 ns. An x-ray streak camera in combination with an x-ray pinhole provides temporally resolved information on target implosions with one-dimensional spatial resolution.

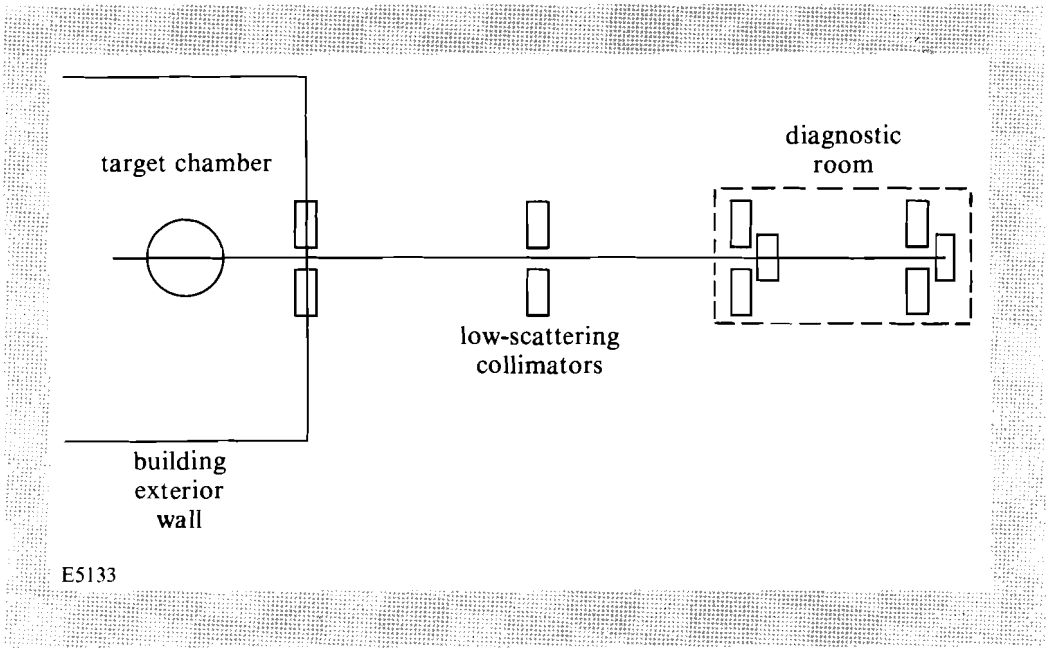

Fig. 39.13
Location of neutron time-of-flight diagnostics outside the present target bay.

Monochromatic x-ray imaging of target implosions is provided by means of a gold x-ray transmission grating in conjunction with an x-ray pinhole camera.

A system for the automatic evaluation of laser pointing on target has recently been developed. It uses a video frame-grabber and microscope to provide an evaluation of the images from several (currently six) views of the target that are provided by x-ray pinhole cameras. Using this system, beams can be reliably positioned to within 15 μrad on the target surface in about one hour. The pinhole cameras in use on OMEGA are located approximately 5 cm from the target. In order to avoid ablation problems, the cameras will be moved to 20 cm on the OMEGA Upgrade, where fluences are equal to that on the present OMEGA system. Resolution at this distance (for silicon x rays) is 25 μm, which is acceptable for targeting: 15 μrad accuracy over 1.8 m corresponds to 27 μm. A similar system will be employed on the upgrade, with more cameras used to allow for accurate placement of all 60 beams.

X-ray spectral-measurement systems, both time-integrated and time-resolved, have been implemented on the current OMEGA system. A novel system incorporating an elliptical crystal and an x-ray streak camera has been developed as a collaborative effort with the NLUF program.[16]

Diagnostic instruments that are in close proximity ($<$20 cm) to the target (pinhole cameras, Kirkpatrick-Baez microscopes, neutron-emission-time detectors, x-ray imaging streak cameras, etc.) will probably experience damage and material ablation under the increased

flux of scattered light, particles, and target debris from the OMEGA Upgrade targets. Moving diagnostics to distances greater than 20 cm, and employing imaging diagnostics with longer image-plane stand-off such as Wolter and Kirkpatrick-Baez microscopes, will assure that they survive.

The OMEGA Upgrade experimental (or diagnostics) control room will be located directly underneath the target chamber, in the area presently housing the diagnostic-control and data-acquisition hardware for the OMEGA system. This location is chosen because of its close proximity to the target chamber. This is important both to save costs and to minimize high-speed signal distortions experienced in long cable lengths. The experimental control room will provide a central data base for the organization of pre-shot and post-shot data, using a local workstation networked to all the other computers of the laboratory. Collection and initial reduction of data from the diagnostic instruments will also be handled by this workstation, in which the CAMAC, General Purpose Interface Bus (GPIB), and RS-232 interfaces will be utilized. Auxiliary terminals and printers will enable prompt inspection and analysis of the data following a target shot, allowing modification of experimental parameters in time for the next target shot. Individual diagnostic instruments will be further controlled locally by smaller computers, to allow for the unloading of various functions from the main workstation controller (these include interlock, vacuum pumps, setup, and protection). Commercial programmable logic controllers are already used for this purpose on some diagnostics on the current OMEGA system.

The prompt nuclear radiation dose projected for the experimental control room may preclude its occupancy during an experiment involving a high-yield DT-fuel target. The networking of the computers in the laboratory will allow the experimental control room to be operated remotely from any location with access to a computer terminal; open access is expected to resume immediately after each shot. The projected silicon dose and dose rate in the present control room is low enough so that upset or damage to any electronic devices will not occur during a shot.

The practices of electromagnetic-interference control that have been successfully adopted for the current OMEGA system will be suitable for the upgrade. The calculated level of electromagnetic interference (EMI) from the upgrade experimental system is no higher than that calculated for the present system, so that additional EMI protection (such as screened rooms, true triaxial or quadraxial cabling, etc.) will not be required.

Nuclear Modeling and Shielding

We have undertaken an extensive joint study with Grumman Aerospace to model the potentially adverse effects of a high level of neutron production on the target chamber and target room, and their surroundings. The modeling employed the one-dimensional discrete neutron-energy-transport code ANISN,[17] in spherical geometry, to study the prompt and activation radioactivity in both silicon

semiconductor devices and biological-tissue samples for several transport scenarios. The modeling used the MONTUK-80 activation-cross-section library, and the MACKLIB-IV response-function library. These data libraries have been developed especially for fusion neutron spectra. The results of the study are given in terms of the prompt dose on silicon and tissue samples, and the nuclear-activation build-up for a typical target-shot schedule.

For the purposes of this study, the relative radiological hazards were determined using health-physics and radiological-dose guidelines from the following sources:

1. Industrial Code Rule 38, Ionizing Radiation Protection (12 NYCRR 38), 1985, State of NY, Department of Labor.
2. Guidelines of the National Council on Radiation Protection and Measurements.
3. Title 10 of the Code of Federal Regulations, part 20 (10CFR20).
4. The "ALARA" (as low as reasonably achievable) recommendation of the International Commission on Radiation Protection.

These sources all quote the following maximum-allowed doses for radiation workers:

1. 3 rem per calendar quarter;
2. total lifetime dose of 5 $(A-18)$ rem, where A is the worker's age in years; and for members of the public:

1. 100 mrem per week;
2. 2 mrem per hour, whole body.

Based on this guideline, an exposure rate of 2.5 mrem/h is sometimes used to establish a dividing line between restricted-access and free-access areas; however, this level is not listed in any of the regulations.

The modeling assumed maximum-credible neutron yields (based on the achievement of ignition as discussed above) as follows:

for a DT shot:
3×10^{15} neutrons of energy 14.1 MeV and 1×10^{13} neutrons of energy 2.45 MeV;

for a DD shot:
1×10^{13} neutrons of energy 2.45 MeV and 5×10^{10} (secondary) neutrons of energy 14.1 MeV.

Such high yields are not anticipated under routine operating conditions; however, it is important to consider the radiological implication of the upgrade project exceeding its goals.

The experimental chamber, turning-mirror structure, optics, building wall, and associated structures were modeled as spherical shells (Fig. 39.14). These shells were dimensioned to reflect the average radius and composition of the actual structures. Thirteen different path configurations for the neutron transport (see Tables 39.VI and 39.VII)

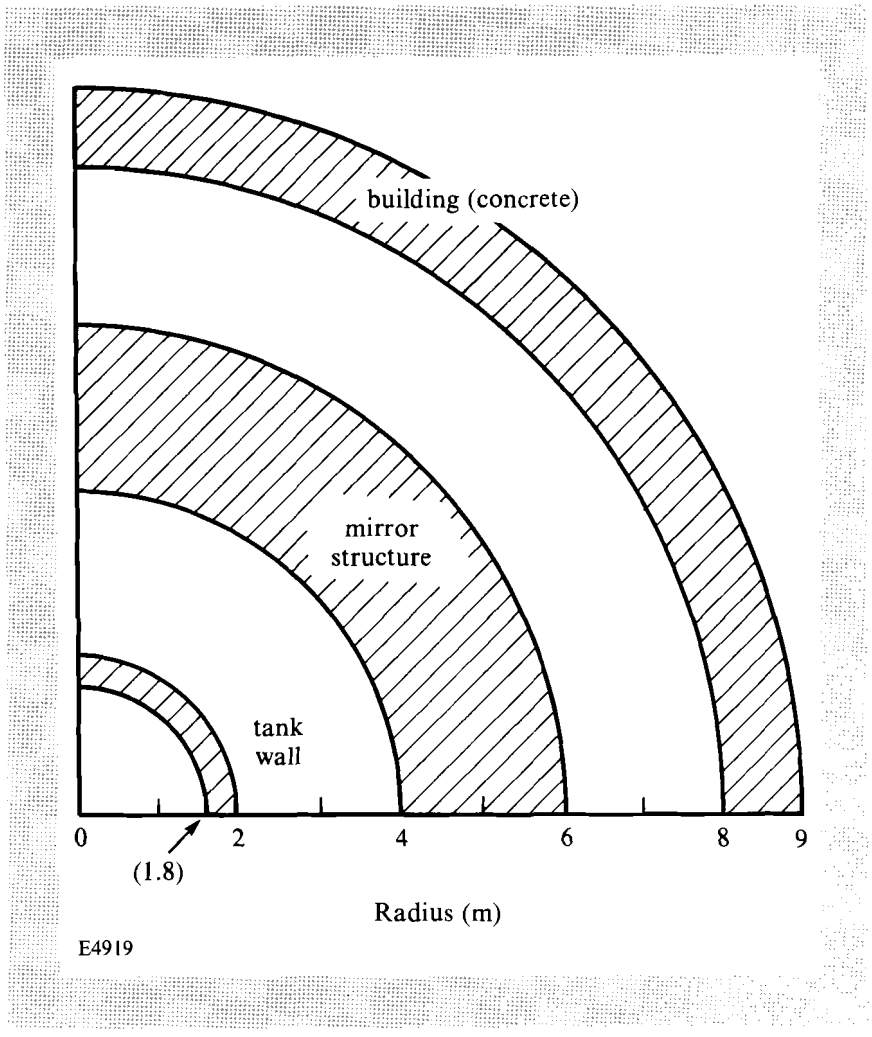

Fig. 39.14
Geometry used for calculating the activation of the target chamber, turning-mirror structure, and building walls.

were modeled. The aluminum components were modeled with aluminum alloy 6061. Since this material has alloying elements that radioactivate more strongly than those in alloy 5083, a worst-case estimate of radioactivity is obtained in the event that some combination of aluminum alloys is used in the final design. The study included the effects on aluminum and steel support structures, and on an assumed experimental chamber constructed of either aluminum or of aircraft titanium of equivalent stiffness. The study assumed that the KDP frequency-conversion crystals would be located near the target, but this option was rejected; the study therefore somewhat overestimates activation levels.

The results of these simulations show that additional shielding will have to be installed in several areas, and some operating procedures will need to be revised in order to limit radiation exposure to personnel. A plan view of the present OMEGA target bay (Fig. 39.15)

Table 39.VI Layer thickness and materials used for ANISN radiation modeling. Layer #1 starts at the target (radius = 0 m).

Geometry	Layer Number			
	1	2	3	4
1	1.8 m vac	10 cm Al	8 m air	
2	1.8 m vac	4.2 m air	5 cm Ti	8 m air
3	6 m air	Optics	Struct. #2	4 m air
4	1.8 m vac	10 cm Al	6.5 m air	Floor
5	1.8 m vac	5 cm Ti	6.5 m air	Floor
6	1.8 m vac	10 cm Al	4.1 m air	Struct. #1
7	1.8 m vac	10 cm Al	4.1 m air	Struct. #1
8	1.8 m vac	5 cm Ti	4.15 m air	Struct. #1
9	1.8 m vac	5 cm Ti	4.15 m air	Struct. #1
10	1.8 m vac	5 cm Ti	4.15 m air	Struct. #2
11	1.8 m vac	5 cm Ti	4.15 m air	Struct. #2
12	1.8 m vac	10 cm Al	4.15 m air	Struct. #2
13	1.8 m vac	10 cm Al	4.15 m air	Struct. #2
	5	6	7	8
1				
2				
3				
4				
5				
6	2.75 m air	Thin wall		
7	2 m air	Thick wall	Thin wall	
8	2.75 m air	Thin wall		
9	Optics	2 m air	Thick wall	Thin wall
10	Optics	2.75 m air	Thin wall	
11	Optics	2 m air	Thick wall	Thin wall
12	Optics	2.75 m air	Thin wall	
13	Optics	2 m air	Thin wall	Thick wall

E5323

shows the lack of adequate shielding along some walls. The use of thick (36–48 in.), movable, keyed, precast-concrete shield blocks in this and other areas that require additional shielding is currently being studied.[18] These blocks are used effectively in high-energy physics laboratories, research reactors, etc. The area directly underneath the target chamber, which presently houses the experimental control area, will have to be operated remotely during a high-yield DT-filled target shot because the prompt tissue dose (30–50 mrem per target shot) would be excessive. The thin-wall building-leakage dose rate (position C on Fig. 39.15) is less than 1 mrem per DT shot with the additional shield walls in place.

Table 39.VII Material terms glossary (used in Table 39.VI)

Al	=	6061 aluminum alloy
Ti	=	aircraft titanium
Optics	=	4 cm fused silica (vacuum window), 7.5 cm fused silica (lens and distributed phase plate), 5 cm KDP (frequency-conversion cell)
Struct. #1	=	5 cm 1040 (mild) steel
Struct. #2	=	7.5 cm Al, 2.5 cm 1040 steel
Thin wall	=	20 cm cinder block, 10 cm brick facia
Thick wall	=	76.2 cm reinforced concrete (reinforcement bars, 1020 mild steel, 1.3-cm diam on 20-cm center-center spacing)
Floor	=	same as thick wall
Air	=	air at atmospheric pressure
Vac	=	vacuum (1×10^{-2} Pa)

E5324

Modeling has further been performed to estimate the effects of the high neutron and *n*-gamma prompt dose rate on electronics and optoelectronics in the vicinity of the experimental chamber. It is likely that within a 20-cm radius of the imploded target, upset and/or permanent damage to electronics will occur. The silicon dose and dose rate for electronics at the wall of the target bay is acceptable for all types of microelectronics, with the exception of power transistors, silicon-controlled rectifiers, and other silicon devices of large junction area. Electronics employing such devices will be transferred to the area beneath the target-bay floor.

Neutron activation of the target chamber, support structure, and surroundings determines the maximum-acceptable number of shots in a given time period, and the minimum time following a target shot, before personnel are allowed reentry into the target bay. Data for a typical activation analysis is presented in Fig. 39.16, for the following experimental scenario:

One DT-fuel target and four D_2-fuel targets per day (2-h shot cycle).

Three days of experiments per week (Monday, Wednesday, and Friday).

Two weeks of experiments, followed by one week of no target shots.

A one-month shut-down period at the end of a 48-week period of experiments.

The modeling follows this cycle for a full year, evaluating the buildup and decay of nuclear products in the target chamber, the support structure, and the exterior wall of the building. Figure 39.16 shows the cycle of activation and decay following each shot for a section of

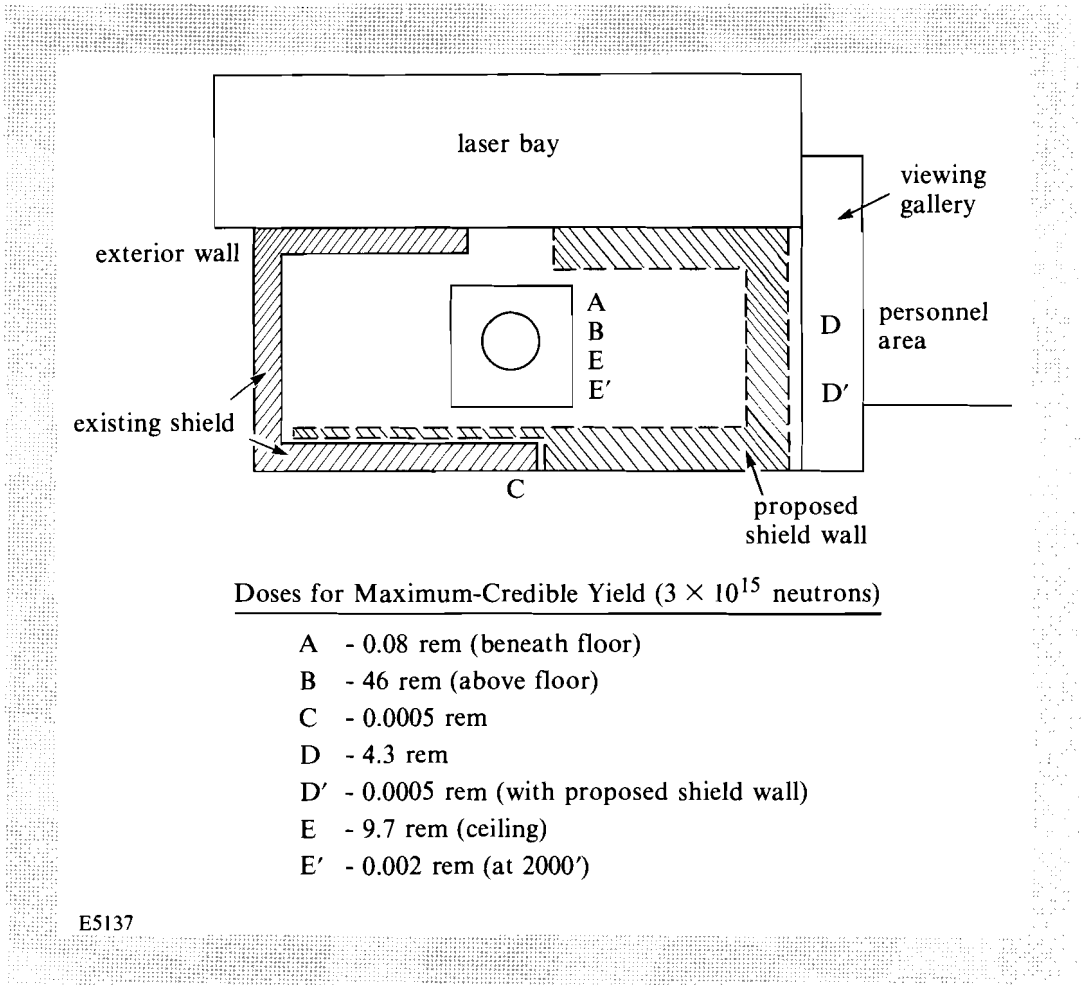

Fig. 39.15
Personnel doses for a DT target shot with a maximum-credible yield of 3×10^{15} neutrons. Location A is in the present diagnostic control room; location E′ is for an aircraft at an altitude of 2000 ft above the target chamber. The shaded areas indicate the location of proposed movable shielding around walls of the target bay.

the thick reinforced cement shield wall modeled on neutron flight paths 7, 11 and 13. For comparison, the normal level of radioactivity for natural cement in this area is about 1×10^{-7} $\mu C/cm^3$. The shield wall represents one of the worst areas for radioactivity because of the long half-life decay products and large mass. Analysis of this data indicates that a "cool down" period of 0.5–1 h between implosion and personnel reentry into the target bay is required.

Nuclear activation of the air in the target bay has also been considered in this study. Following a high-yield DT-filled target shot, the air in the vicinity of the target chamber will be activated to about 15 $\mu C/m^3$ (due to the activation of the nitrogen isotope N^{13}, which decays with a half-life of 9.95 min). Activation of the air to this level will require an extension of the cool-down cycle duration.

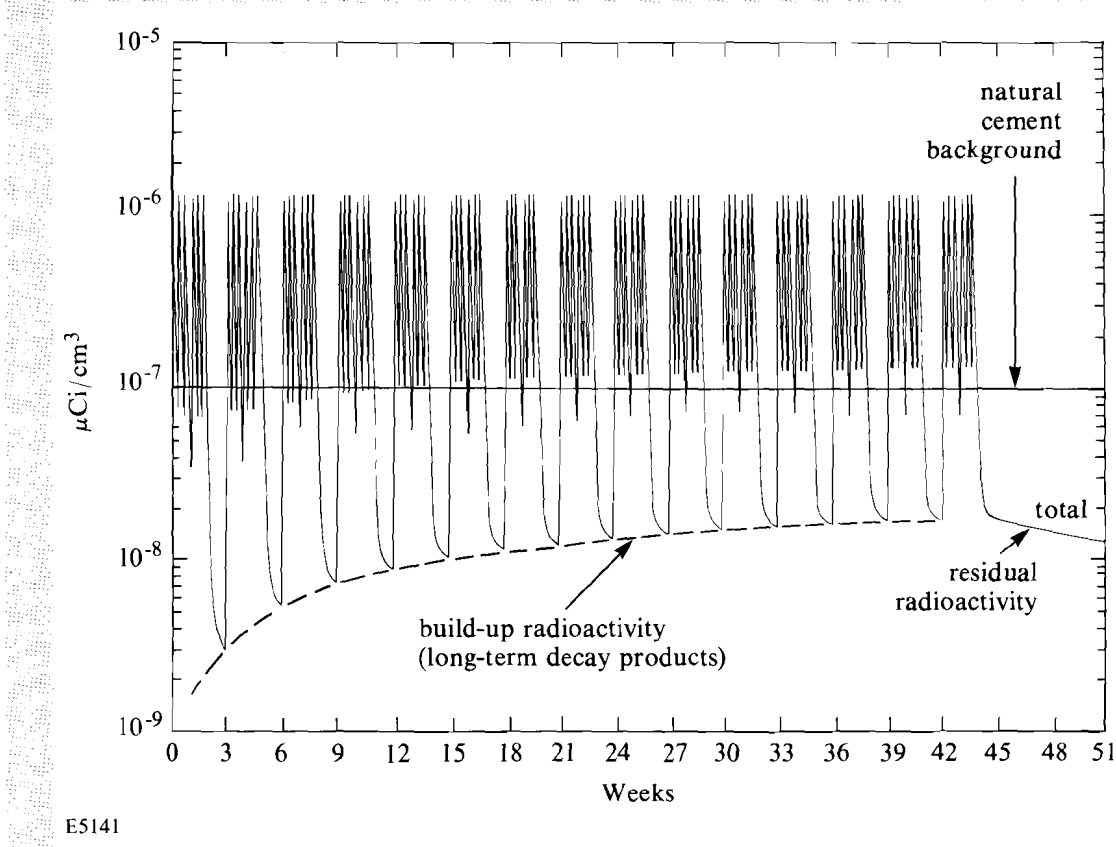

Fig. 39.16
Activation analysis of the shield-wall material for a projected year of experiments, showing the buildup and decay of radioactive products at the exterior wall for the assumed daily, weekly, and yearly schedule. The spikes are due to short half-life radionuclides, primarily from the reaction Na^{23} (n,γ) Na^{24}. The build-up residual radioactivation is due to the longer half-life reactions Ca^{40}(n,α) Ar^{37}, K^{39} (n,T) Ar^{37} and Ca^{44}(n,γ) Ca^{45}.

Because of the low-level radiation hazard that may exist following an implosion involving thermonuclear reactions, radiation-monitoring equipment will be installed in the target bay, air plenums, and in adjacent areas, to monitor the prompt and activation doses. The monitoring equipment will include tritium (beta-decay) detectors placed near the target bay to check for radioactivity of diagnostic instruments outside the experimental chamber; prompt neutron and gamma-ray total-dose detectors (calorimeters) placed in the target bay and nearby areas; and filtration-type air-sampling equipment for monitoring air activation in the plenums leading to and from the target bay. Similar detectors will be located in the areas of the laser bay that are unshielded and in proximity to the target chamber. These detectors will be connected to computer-controlled interlocks, in order to eliminate the possibility of inadvertent entry of personnel during cool-down periods. These precautions will allow operation at the maximum shot rate consistent with personnel safety.

ACKNOWLEDGMENT

This work was supported by the U.S. Department of Energy Office of Inertial Fusion under agreement No. DE-FC03-85DP40200 and by the Laser Fusion Feasibility Project at the Laboratory for Laser Energetics, which has the following sponsors: Empire State Electric Energy Research Corporation, New York State Energy Research and Development Authority, Ontario Hydro, and the University of Rochester. Such support does not imply endorsement of the content by any of the above parties.

REFERENCES

1. J. F. Figueira and S. J. Thomas, *IEEE J. Quantum Electron.* **QE-18**, 1381 (1982).
2. J. H. Nuckolls, Lawrence Livermore National Laboratory Report UCRL-84932 (1980).
3. Y. P. Raizer, *Sov. Phys. JETP* **21**, 1009 (1965).
4. LLE Review **33**, 11 (1987).
5. LLE Review **27**, 103 (1986).
6. LLE Review **36**, 150 (1988).
7. R. Kremens and M. Russotto, presented at the 31st Annual APS meeting of the Plasma Physics Division, Anaheim, CA, 13-17 November 1989.
8. M. D. Cable, *J. Appl. Phys.* **60**, 3068 (1988).
9. D. R. Welch, H. Kislev, and G. H. Miley, *Rev. Sci. Instrum.* **59**, 610 (1988).
10. D. R. Kania *et al.*, *IEEE Trans. Nucl. Sci.* **35**, 387 (1988).
11. C. L. Wang *et al.*, *Rev. Sci. Instrum.* **57**, 1749 (1986).
12. G. L. Tietbohl, R. A. Lerche, and S. M. Lane, *Bull. Am. Phys. Soc.* **33**, 1868 (1988).
13. J. D. Kilkenny *et al.*, *Rev. Sci. Instrum.* **59**, 1793 (1988).
14. D. K. Bradley, J. Delettrez, P. A. Jaanimagi, F. J. Marshall, C. P. Verdon, J. D. Kilkenny, and P. Bell, *High Speed Photography, Videography, and Photonics VI* (SPIE, Bellingham, WA, 1988), Vol. 981, p. 176.
15. P. E. Bell, J. D. Kilkenny, G. Power, R. Bonner, and D. K. Bradley, *Ultra High Speed, High Speed Photography and Videography and Photonics VII* (SPIE, Bellingham, WA, 1989), to be published.
16. B. L. Henke and P. A. Jaanimagi, *Rev. Sci. Instrum.* **56**, 1537 (1985).
17. ANISN, Oak Ridge National Laboratory.
18. Radiological Safety in the Design and Operation of Particle Accelerators, NBS Handbook 107, revised 1978, U.S. Department of Commerce.

Section 2
ADVANCED TECHNOLOGY DEVELOPMENTS

2.A Interaction of Picosecond Optical Pulse with High-Temperature Superconductors

The recently discovered high-temperature, ceramic oxide superconductors present new possibilities for optical detectors and opening switches.[1-5] The viability of these applications depends on the nature of optical interactions and resulting microscopic energy transport within these materials, and how the superconducting electrical properties are thereby affected. Several models have been proposed[6-8] to explain experimental observations on the oxide superconductors, but the full picture remains somewhat murky. The major contention appears to be whether the optical response is predominantly bolometric (i.e., thermal), or alternatively due to some other, perhaps nonequilibrium mechanism.

We have investigated the transient electrical response of $YBa_2Cu_3O_7$ (YBCO) superconducting films irradiated with fast optical pulses from a Nd:YAG laser. The pulses are about 100 ps long, and the temporal resolution of the sampling scope is about 1 ns, fast enough to distinguish thermal and nonthermal processes. We show below that, although the magnitude of the signal corresponds to simple heating, nonequilibrium energy transport must be playing a part in distributing the heat through the thickness of the film.

A parallel motivation for our experiments has been to assess the feasibility of a high-T_c film as the active element in an optically triggered high-current opening switch. In such a switch, a superconducting current shunt is illuminated by a fast optical pulse.

The superconductor is then rapidly converted into a high-resistance (normal) conductor, diverting the current into the desired load. Potential applications include pulsed-power systems[9] and fault-current limiters.[10] Several features of oxide superconductors are attractive for such a device, including low optical reflectivity, large absorption depth, high normal-state resistance, moderate operating temperatures (77°K), and potentially large currents (up to ≈ 10 MA/cm^2). A switch 1 μm thick and 1 cm wide would be able to carry 1 kA. Our measurements reported here indicate that the most important requirement, fast switching (on the nanosecond scale or less), can also be met in these films.

Opening switches are interesting because they can be used in conjunction with inductive electrical storage devices such as superconducting magnets. As shown in Fig. 39.17, the opening switch is placed in series with the inductor and, when the switch opens, the current is diverted to the load. At the present time there are very few fast electronic opening switches. Most electronic switches are closing switches that can only be used with capacitive storage systems. An additional advantage of a superconducting opening switch is that it would not introduce losses in the inductive charging circuit.

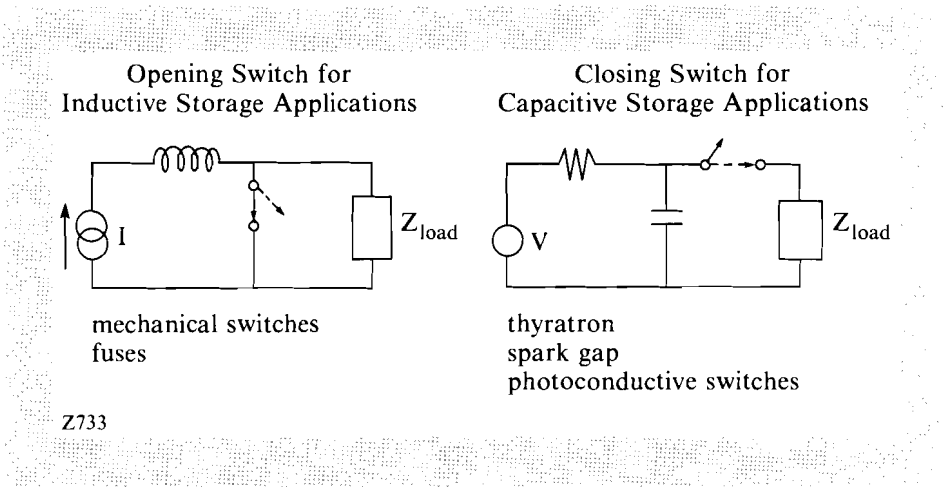

Fig. 39.17
Opening and closing switch configurations.

Sample Preparation

The superconducting films for this study were deposited (by personnel at CVC Products of Rochester, NY) using rf magnetron sputtering from a single stoichiometric $YBa_2Cu_3O_7$ target onto polished yttria-stabilized zirconia single-crystal substrates, yielding films of similar composition.[11] After an *ex-situ* anneal to 850°C followed by a slow cool in oxygen to convert completely to the superconducting state, the films consisted of randomly oriented grains ≈ 1 μm across for a 1-μm-thick film.

In order to carry out quantitative electrical measurements on the films, we have used a scanned focused laser beam to ablate parts of the film and thereby pattern device structures.[12] The laser was the same one used for the laser switching described below: a pulsed Nd:YAG laser with regenerative amplification, with 100-ps pulses at

1.064 μm and a repetition rate of 1 kHz. A single pulse with 10 μJ of energy, focused down to a 20- to 40-μm spot (a fluence of 1 to 10 J/cm^2), could etch through a 1-μm-thick film. By scanning the sample at $\approx$1 mm/s, we could etch line across the film. The samples used for the transient response studies consisted of an *H* structure with a central bridge region 263 μm wide and 2.5 mm long.

Low-resistance contacts (about 1 Ω) were obtained by evaporating 0.2 μm of Ag on top of the YBCO films, and then wire-bonding to the Ag pads. The dc resistive transition of the bridge region of a 0.7-μm-thick film is shown in Fig. 39.18 for two different measuring currents, together with the temperature dependence of the superconducting critical current (defined by a voltage of 1 μV). Note that the normal-state resistance is only weakly dependent on temperature. This sample is not optimized, exhibiting a broadened transition ($R = 0$ only below 60°K) and relatively low critical-current density (<1 kA/cm^2 at low T). Thicker films (>1 μm) generally exhibited much better superconducting performance, as did films prepared on epitaxial substrates or by deposition at higher temperatures. Still, as we indicate below, this nonideal granular film showed a strong optical response over a wide range of temperatures, currents, and laser powers. The data presented in this paper will primarily focus on the film of Fig. 39.18, but data will also be presented on thicker and thinner film as well as films on $SrTiO_3$.

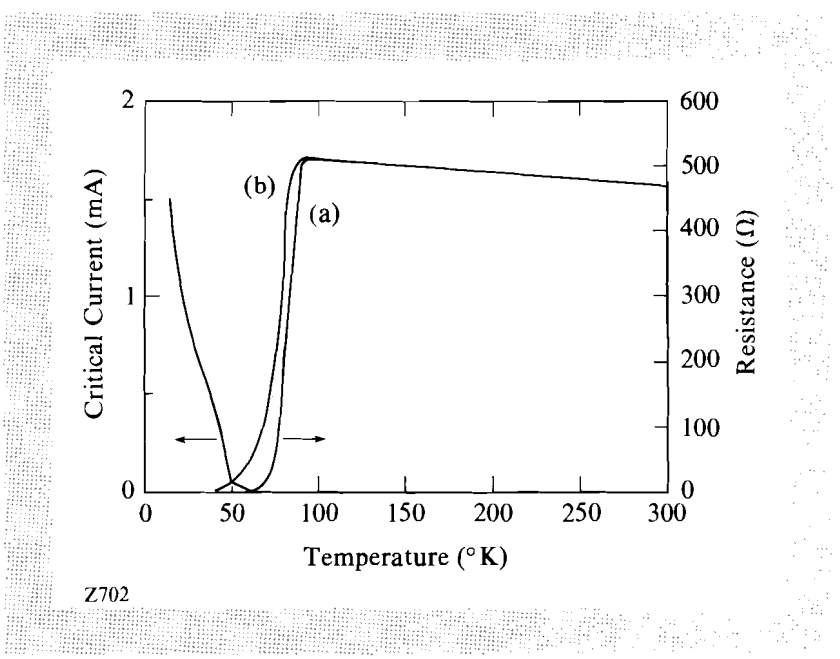

Fig. 39.18
Temperature dependence of dc resistance $R(T)$ for superconducting YBCO film #216 using two measuring currents, (a) I = 10 μA and (b) I = 1 mA. The dimensions of the region tested were 2 mm long × 200 μm wide × 0.7 μm thick. Also plotted is the critical current $I_c(T)$.

Experimental Procedure

For the pulse-excitation measurements (see Fig. 39.19), the sample was mounted in vacuum in a continuous-flow He Dewar, on a stage whose temperature could be controlled from 10°K to 100°K or higher. The switch was illuminated (from the top of the film) through a quartz window with a 3-mm-wide beam from the Nd:YAG infrared laser with

100-ps pulses, each with up to 100 μJ of energy, at a repetition rate of 50 Hz.

The switch was provided with a dc bias (typically 0.1 to 5 mA) across its legs, and the voltage across the two others was connected to a terminated 50-Ω coaxial line, which was measured with either a fast-analog or a digital-sampling oscilloscope. Care was taken to eliminate possible transmission-line reflections in the circuit. Data was recorded with a 200-MHz digital oscilloscope. The rise time was measured with a 350-MHz fast-analog scope.

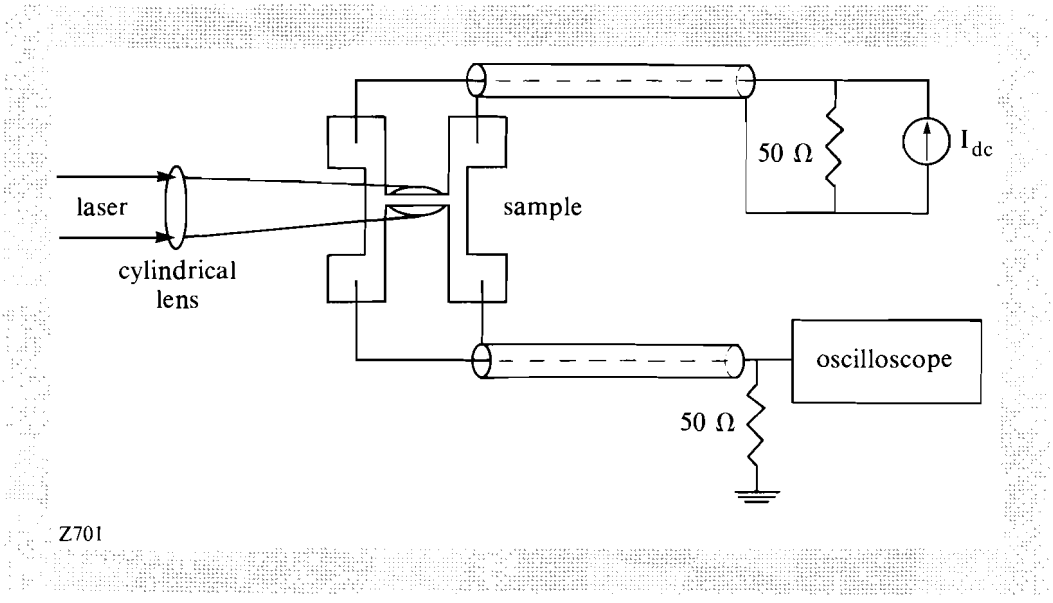

Fig. 39.19
Schematic of the experimental setup for pulsed-laser excitation of superconducting thin-film sample.

An example of the transient response of the sample to a 150-ps laser pulse is shown in Fig. 39.20, on the 10-ns time scale. Since the full normal-state resistance of the switch was about 500 Ω, much greater than the 50-Ω line impedance, a parallel combination of the two was measured. The data were taken for $T = 17°K$, for a current $I = 2$ mA and incident fluences of 0.53, 2.1, and 6.7 mJ/cm^2. The nonzero voltage on the left results from the use of a two-point probe, thus including the contact resistance in the baseline measurement. After illumination the load resistor experiences a sharp rise in voltage in about 2 ns, a slower rise in voltage on the scale of 10 to 100 ns (missing in some cases), and a slow decay back to the background level with a characteristic time of about 1 μs. The fast rise and slow relaxation on these time scales were present for all parameters studied. The measured rise time was limited by dispersion in the measurement circuit.

Results and Discussion

In Fig. 39.21 we plot the magnitude of the fast voltage rise versus the laser fluence, together with results of a simple heating model

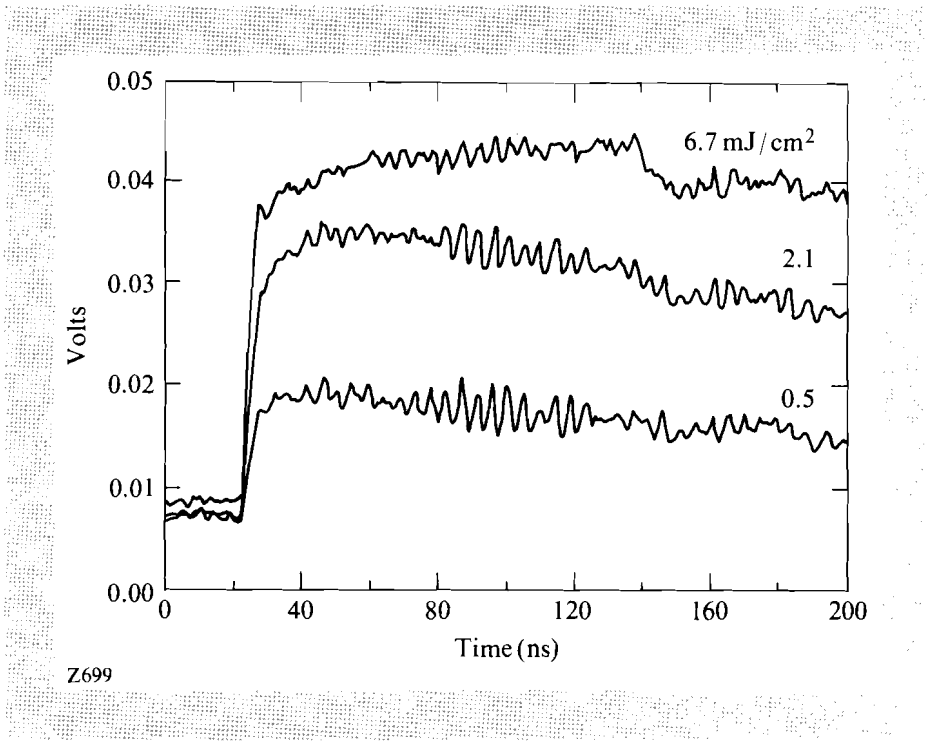

Fig. 39.20
Transient response of sample #216 to a 150-ps optical pulse, for several values of laser fluence, for $T = 17$ °K and $I = 2$ mA. The switching time ≈ 2 ns was identified on a faster analog scope.

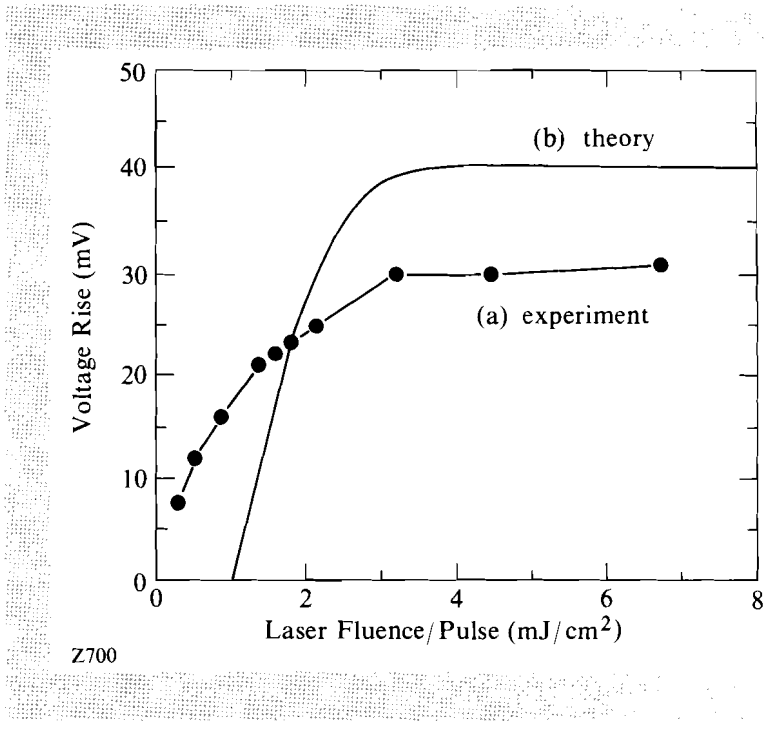

Fig. 39.21
Dependence of the fast transient voltage rise on laser fluence. (a) Experimental measurements, for $T = 17$ °K and $I = 2$ mA. (b) Theoretical results of a simple heating model assuming uniform distribution of energy through the film thickness.

where we assume the optical energy is uniformly distributed throughout the film. The switch was assumed to attain a resistance given by the resistance versus temperature curve in Fig. 39.18. Above a fluence of about 2 mJ/cm^2 per pulse, the voltage saturates, corresponding to switching the full normal-state resistance.

The optical-absorption depth for the YBCO film was measured using a spectrophotometer and found to be about 120 nm, only weakly dependent on wavelength. This is consistent with other reports in the literature.[13] Since the films are much thicker than this, the optical energy is initially deposited almost entirely in the top 200 nm of the film. If the effect of the light was simply to drive the top layer of the superconducting film into the normal state, an initial voltage would fall as soon as the current could divert into a deeper layer of the film that is still superconducting (the films should be superconducting down to the substrate, particularly at low T). This would be the case whether the current was flowing uniformly or was restricted to the surface by superconducting screening. This current redistribution should occur much faster than the equilibrium heat flow (see below). A straightforward application of Maxwell's equations shows that field penetration into a conductor (essentially the ac skin-depth problem) occurs by a diffusive process with a characteristic electromagnetic diffusivity $D_{em} = \rho/\mu_o \approx 10^5$ cm^2/s, where $\rho \approx 1$ mΩ·cm is the normal resistivity of this film. This value corresponds to approximately 1 fs for current to divert around a normal layer $\approx$100 nm thick, much faster than our temporal resolution, and can clearly not account for the 1-μs decay we observe.

Equilibrium thermal transport is governed by the thermal diffusivity $D = K/C$, where K is the thermal conductivity and C the heat capacity (per unit volume). These were not measured for these films, but an upper estimate of K at 25°K (for a single crystal) is of order 0.01 W/cm°K, and that for C at a similar temperature is 0.1 J/cm^3°K.[14] These correspond to $D \approx 0.1$ cm^2/s, or diffusion of 30 nm in 100 ps and 300 nm in 10 ns. Clearly, in less than 2 ns, the heat cannot have spread throughout a 700-nm film. We are therefore forced to conclude that, on the nanosecond time scale, the heat is distributed essentially uniformly throughout a 0.7-μm film.

The estimates made above have been verified by modeling the thermal transport with finite-element code. The energy absorbed per unit length was deduced from the optical-absorption length. The initial temperature distribution was determined by integrating:

$$dE_{\text{absorbed}}(x)/dx = \rho \int_{T_0}^{T_f} C_p(T)dT$$

where $C_p(T) = 0.0028T$–0.04 (J/cm°K) and is determined from a fit to the data in Ref. 14. ρ is the linear mass density and dx is the incremental length, using a thermal conductivity of 5×10^{-3} W/°K cm^2. These values were used to solve the one-dimensional heat equation. Figure 39.22 shows the time evolution of the temperature profile for the case of insulated boundary conditions. This case will underestimate the time necessary for the entire thickness of the material to rise above T_c because it ignores the heat lost to the substrate. This figure shows that the temperature changes very little in 2 ns and takes 50 ns to rise above T_c at the back of the film. The

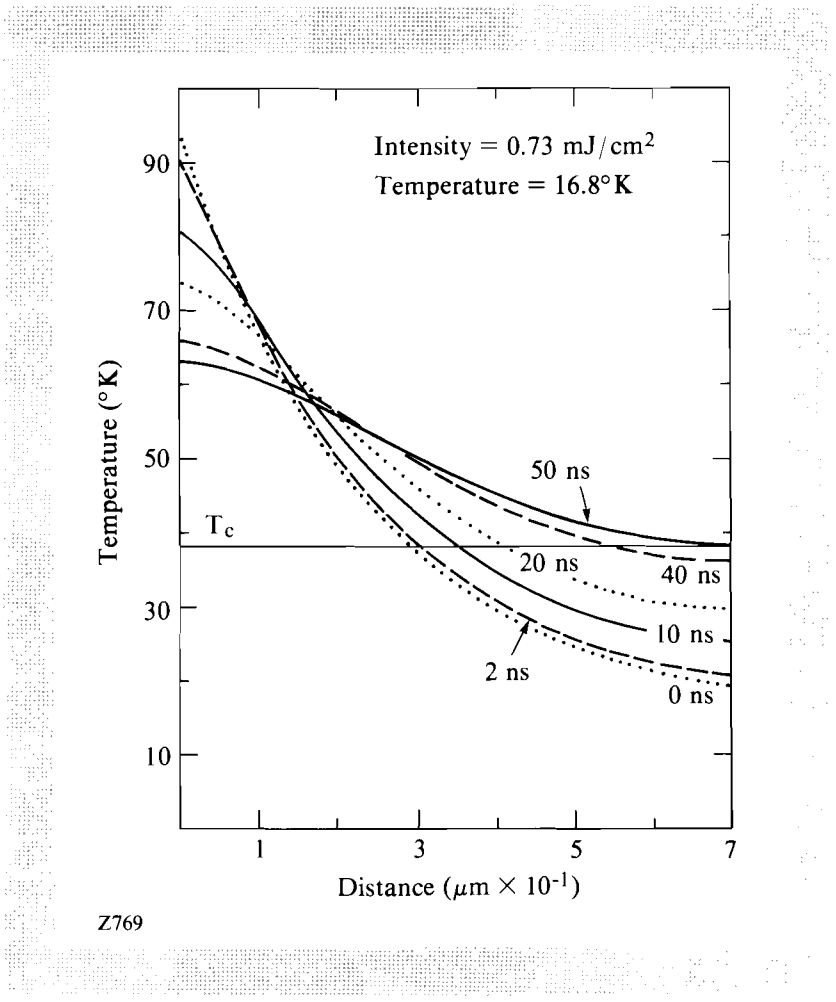

Fig. 39.22
Time evolution of the temperature profile of a 0.7-μm YBCO film.

actual voltage rise time measured for the case illustrated in Fig. 39.22 was less than 2 ns. This was indicative of all the points illustrated in Fig. 39.21 whether or not the optical energy was sufficient to drive the entire film normal at zero time. Clearly thermal transport cannot account for the fast rise times that we observe.

If neither optical absorption nor equilibrium heat flow is capable of distributing this energy, then an alternative nonequilibrium mechanism must be responsible. We suggest that hot-electron transport, which has previously been demonstrated for optically excited metals such as Cu and Au,[15,16] is likely to provide part of the answer. The initial effect of the radiation is to create a number of highly excited electrons and holes in the top 100 nm of the film. These distribute their energy among other highly excited electrons, which spread, either ballistically or diffusively, penetrating into the film. They then thermalize with the lattice (due to the electron-phonon interaction) in a relaxation time that is likely to be a few picoseconds. For an electron diffusivity of order 10^3 cm^2/s, this corresponds to just under 1-μm penetration. Future studies will determine whether these are reasonable estimates, and whether they depend significantly on temperature.

Despite the proposed nonequilibrium energy transport, the voltage rise following the switching appears to be consistent with a bolometric (i.e., thermal) response. This is evident from the dependence of the voltage rise on laser fluence, which we plot in Fig. 39.21 together with the theoretical dependence predicted by a simple heating model. Despite the approximations in the analysis, the experimental and theoretical curves in Fig. 39.21 agree in general magnitude and shape (without any adjustable parameters), and in particular in the fluence (3 mJ/cm^2) at which saturation occurs.

In addition, the rise on the 10-ns scale (see Fig. 39.20) that immediately follows the faster jump is consistent with a redistribution of some heat towards the back of the film, perhaps because the hot-electron penetration depth is comparable to the film thickness. The final slow recovery ≈ 1 μs appears to be due to heat flow out of the film into the substrate. A thinner film should have a much faster cooling time, especially in combination with a well-matched substrate and a transparent top layer to carry away heat, since the thermal-relaxation time goes as the square of the thickness.

Furthermore, we have carried out preliminary measurements on both a thicker and a thinner YBCO film (1.5 μm and 0.2 μm). The general results on these films are also consistent with the above picture of a fast voltage rise on the nanosecond scale, followed by a slow decay that corresponds to thermal conduction out of the film. However, Fig. 39.23 shows data from a YBCO film on $SrTiO_3$. The rise time of the voltage pulse was 20 ns. This is approximately the time of thermal transport. It is unclear whether the physics of the absorption mechanism is different or whether the high dielectric constant of the substrate ($\epsilon \approx 1000$) is influencing the rise time. The film does have higher transition as shown in Fig. 39.24.

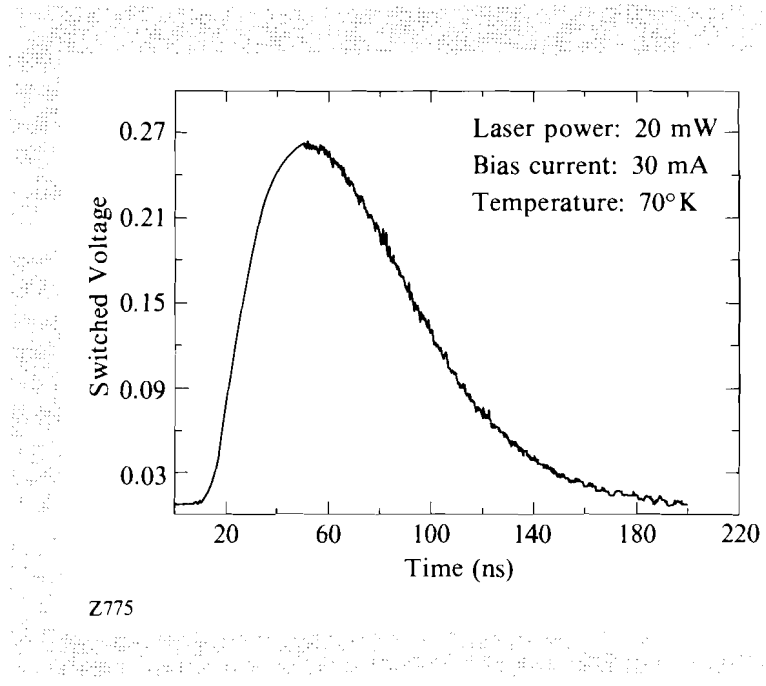

Fig. 39.23
Transient response of YBCO on $SrTiO_3$.

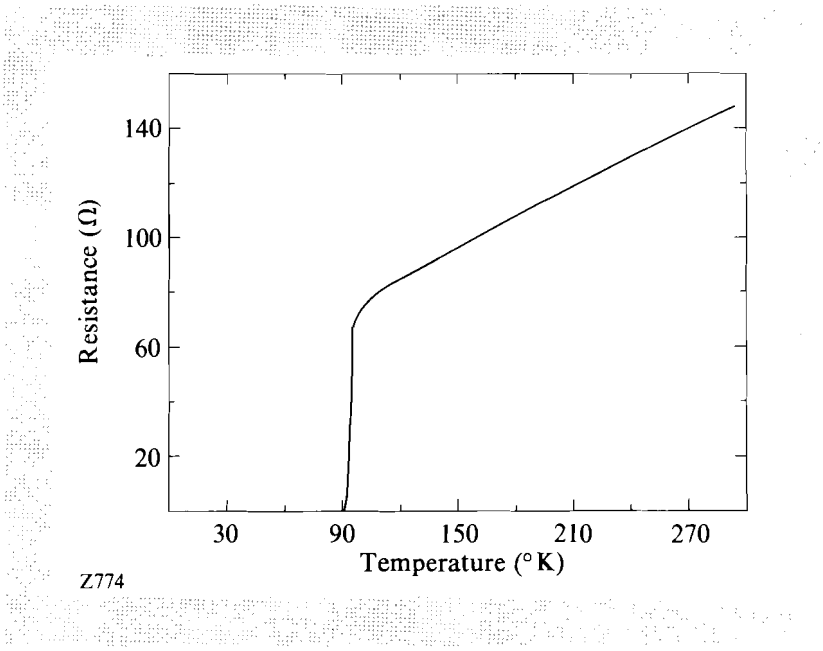

Fig. 39.24
Resistance versus temperature of YBCO on $SrTiO_3$.

We did not concentrate on the low-power limit for this study, so that we have not clearly identified threshold effects. However, extrapolation of our data to zero light intensity indicates the absence of a threshold level that is in marked contradiction to the purely bolometric response. If this is indeed the case, this may indicate a nonequilibrium response where the effect of the light is to break the Cooper pairs rather than heat the lattice.

Although our measurements to date have included only granular films, we would anticipate that epitaxial YBCO films would switch in a similar time. An epitaxial film would have a much larger critical current, so that switching of larger currents (amps instead of milliamps) would become possible, although self-heating would then become relevant.

In summary, we have shown that a 150-ps optical pulse illuminating a high-temperature superconducting film, even one as thick as ≈ 1 μm, can induce a very rapid transition from the superconducting to the normal state, in a time of order 1 ns or less. Switching back to the superconducting state tends to be much slower, of order 1 μs or longer. We can understand this behavior in terms of a model in which the heat is initially deposited in an optical penetration depth ≈ 100 nm at the top of the film, but rapidly spreads (in several ps) via nonequilibrium hot electrons an additional distance of order 1 μm. These then thermalize with the lattice, and for a 150-ps optical pulse, produce an essentially bolometric response on this same time scale. The cool-down process is much slower, however, since it involves equilibrium thermal conductivity (via phonons) out of the film into the substrate.

These characteristics are highly encouraging for potential application to an optically triggered opening switch, particularly if similar results

can be obtained using films with higher critical currents. The existence of this nonequilibrium mechanism suggests that even faster switching, down to the picosecond scale, may be possible for shorter optical pulses. The fact that fast switching occurs in optically thick film means that large currents can be switched on rapid time scales because the film thickness does not limit the switching time.

ACKNOWLEDGMENT

This work was supported by the Laser Fusion Feasibility Project at the Laboratory for Laser Energetics, which has the following sponsors: Empire State Electric Energy Research Corporation, New York State Energy Research and Development Authority, Ontario Hydro, and the University of Rochester; and by AFOSR under contract No. 84-175. Such support does not imply endorsement of the content by any of the above parties.

REFERENCES

1. M. G. Forrester, M. Gottlieb, J. R. Gavaler, and A. I. Braginski, *Appl. Phys. Lett.* **53**, 1332 (1988); *IEEE Trans. Magn.* **MAG-25**, 1327 (1989).
2. M. Leung *et al.*, *Appl. Phys. Lett.* **51**, 2046 (1987).
3. P. L. Richards, S. Verghese, T. H. Geballe, and S. R. Spielman, *Appl. Phys. Lett.* **54**, 283 (1989); *IEEE Trans. Magn.* **MAG-25**, 1335 (1989).
4. M. Wautelet, *J. Phys. D* **20**, 1318 (1987).
5. T. L. Francavilla *et al.*, *IEEE Trans. Magn.* **MAG-25**, 1996 (1989).
6. Y. Enomoto and T. Murakami, *J. Appl. Phys.* **59**, 3807 (1986).
7. U. Strom *et al.*, *IEEE Trans. Magn.* **MAG-25**, 1315 (1989).
8. J. Talvacchio, M. G. Forrester, and A. I. Braginski, to be published in *Science and Technology of Thin-Film Superconductors* (Plenum, New York, 1989).
9. D. R. Humphreys, T. L. Francavilla, D. U. Gubser, and S. A. Wolf, in *Proceedings of IEEE International Pulsed Power Conf.*, 279 (1987).
10. K. E. Gray and D. E. Fowler, *J. Appl. Phys.* **49**, 2546 (1978).
11. A. M. Kadin, P. H. Ballentine, J. Argana, and R. C. Rath, *IEEE Trans. Magn.* **MAG-25**, 2437 (1989).
12. P. H. Ballentine, A. M. Kadin, M. A. Fisher, D. S. Mallory, and W. R. Donaldson, *IEEE Trans. Magn.* **MAG-25**, 950 (1989).
13. I. Bozovic *et al.*, *Phys. Rev. Lett.* **59**, 2219 (1987).
14. H. E. Fischer, S. K. Watson, and D. G. Cahill, *Comments on Condensed Matter Physics* **14**, 65 (1988).
15. P. B. Corkum, F. Brunel, N. K. Sherman, and T. Srinivasan-Rao, *Phys. Rev. Lett.* **61**, 2886 (1988).
16. S. D. Brorson, J. G. Fujimoto, and E. P. Ippen, *Phys. Rev. Lett.* **59**, 1962 (1987).

Section 3
NATIONAL LASER USERS FACILITY NEWS

During the third quarter of FY89 NLUF activity consisted of support for work done by **J. Seely** of NRL, **C. Hooper** of the University of Florida, **A. Honig** of Syracuse University, and **P. Cheng** of SUNY Buffalo, and preparation for acceptance of new FY90 proposals at the DOE San Francisco office.

J. Seely visited LLE to take data on Au-coated targets with the 3-m grazing-incidence spectrograph. The XUV spectrum from this target was used to calibrate the thickness of foils placed in the spectrograph. Data were taken for 800-μm-diameter targets and 250-μm-diameter targets. The beams on the larger target were well separated; thus, the illumination intensity was reduced by a factor of 5. The 3-m spectrograph has been taken to LLNL for a series of measurements NRL is doing with the NOVA laser.

C. Hooper visited LLE to plan for future collaborative experiments with Ar-gas implosions. These experiments will use the OMEGA laser to implode Ar-filled plastic shells and Ar-doped D_2-filled shells to study high-density plasmas. Target selection, diagnostic instrumentation, analysis, and scheduling were discussed during this visit.

A. Honig visited to finalize plans for a FY90 NLUF proposal. The group from Syracuse has demonstrated the ability to freeze polarized D_2 and is now working on a technique to insert a frozen target into

the OMEGA target chamber. This will facilitate the implosion of cryogenic targets at any ICF laboratory.

P. C. Cheng is collaborating with LLE to do x-ray microradiography using a GDL-created plasma as an x-ray source. Both biological and inert material have been exposed to the x-ray fluence. The data have been taken to SUNY Buffalo for further analysis.

ACKNOWLEDGMENT

This work was supported by the U.S. Department of Energy Office of Inertial Fusion under agreement No. DE-FC03-85DP40200.

Section 4
LASER SYSTEM REPORT

4.A GDL Facility Report

During the third quarter of FY89 the experimental program in GDL consisted of four separate efforts. Laser shots were dedicated to continuance of the following projects: shine-through, x-ray laser, and x-ray microscopy. This quarter also marked the deployment of a short ($\sim$20-ps) pulsed probe beam. The shine-through experiments continued investigation of early-time phenomena in laser-produced plasmas, in particular the transmission of light through a target before the generation of plasma. The x-ray laser program continued investigating both the collisional excitation laser and a resonant photopumping scheme. In addition, one shot day (six shots) was dedicated to a joint experiment with the University of Maryland for plasma spectroscopy for x-ray lasers. The x-ray microscopy experiments are aimed at identifying a biological source of pure silicon. The probe beam that has been directed to the GDL target-irradiation facility will be used in two ways: first, as a backlight source (= 527 nm) for an imaging system that will investigate plasma generation and expansion; second, as a pump beam for Thomson-scattering experiments.

The engineering and technical staff in GDL have continued their support of the OMEGA fusion campaign. One aspect of that support was the characterization of 24 KDP conversion cells for the OMEGA laser. During this quarter, an acousto-optic Q-switch was installed in the GDL oscillator providing more stability to the laser operation. Lastly, some film-calibration studies were performed in GDL.

A summary of the GDL operation is as follows:

Beamline Test, Calibration, Tuning and Laser Alignment Shots	96
Target Shots	
Shine-through	28
X-Ray Laser	47
X-Ray Lithography	13
KDP Characterization	53
Film Calibration	5
TOTAL	242

4.B OMEGA Facility Report

During this quarter, the OMEGA laser facility returned to full-time operation as a target-irradiation facility. In addition, the programs for spatial smoothing by spectral dispersion (SSD) and power balance were continued. The SSD subsystem is now routinely operational, and a comprehensive beam characterization program was carried out to optimize the beam-smoothing parameters. A number of system modifications were implemented to improve the beam energy and power balance.

To assure optimum performance, each target-shooting day a pointing test shot was taken and was followed by frequency-conversion tests. Laser-to-target pointing accuracy was measured using x-ray pinhole camera photography from high-energy target shots on 800-μm gold-coated glass microballoons. On a typical pointing shot, six re-entrant cameras were deployed giving views of all beams on the target. All six images were immedately developed, digitized, and analyzed to determine the positions of the beam on target. Actual positions were compared to the calculated locations by a software routine that determined the beam positions to ± 5 μm. Beams further than 10 μm from the calculated best position were adjusted using the final transport mirror. The pointing data reduction was normally accomplished in 1 h.

In summary, the laser has delivered a large number of well-characterized and uniform irradiation shots on target. The following shot summary reflects the increased number of laser test shots currently required to achieve the high level of precision and uniformity, but steps are being taken to reduce the system time required for laser tuning and calibration.

A synopsis of laser shots for this quarter follows:

Driver Line	139
Laser Test	317
Target	138
Software Test/Other	84
TOTAL	678

PUBLICATIONS AND CONFERENCE PRESENTATIONS

Publications

W. R. Donaldson, A. M. Kadin, P. H. Ballentine, and R. Sobolewski, "Interaction of Picosecond Optical Pulses with High T_c Superconducting Films," *Appl. Phys. Lett.* **54**, 2470–2472 (1989).

R. L. McCrory and J. M. Soures, "Inertially Confined Fusion," in *Laser-Induced Plasmas and Applications,* edited by L. J. Radziemski and D. A. Cremers (Marcel Dekker, Inc., New York, 1989), pp. 207–268.

R. L. McCrory, J. M. Soures, C. P. Verdon, F. J. Marshall, S. A. Letzring, T. J. Kessler, J. P. Knauer, H. Kim, R. L. Kremens, S. Skupsky, R. L. Keck, D. K. Bradley, W. D. Seka, P. A. Jaanimagi, J. A. Delettrez, and P. W. McKenty, "High-Density, Direct-Drive Implosion Experiments," in *Laser Interaction With Matter,* edited by G. Velarde, E. Minguez, and J. M. Perlado (World Scientific, Singapore, New Jersey, London, and Hong Kong, 1989), pp. 73–78.

A. Simon and R. W. Short, "Energy and Nonlinearity Considerations for the Enhanced Plasma Wave Model of Raman Scattering," *Phys. Fluids B* **1**, 1073–1081 (1989).

A. Simon and R. W. Short, "Comments on 'Studies of Raman Scattering from Overdense Targets Irradiated of Several Kilojoules of 0.53-μm Laser Light'," *Phys. Fluids B* **1**, 1341–1342 (1989).

M. D. Skeldon and R. W. Boyd, "Transverse-Mode Structure of a Phase-Conjugate Oscillator Based on Brillouin-Enhanced Four-Wave Mixing," *IEEE J. Quantum Electron.* **25**, 588–594 (1989).

J. P. Apruzese, P. G. Burkhalter, J. E. Rogerson, J. Davis, J. F. Seely, C. M. Brown, D. A. Newman, R. W. Clark, J. P. Knauer, and D. K. Bradley, "Enhanced Excitation and Ionization of Neonlike Silver in Laser-Produced Plasmas Simultaneously Irradiated by Two Wavelengths," *Phys. Rev. A* **39**, 5697–5704 (1989).

Y. F. Maa and S. H. Chen, "Synthesis of Thermotropic Liquid Crystalline Side-Chain Polymers via Chemical Modification of Polymeric Carboxylic Acids," *Macromolecules* **22**, 2036–2039 (1989).

E. J. Miller, M. D. Skeldon, and R. W. Boyd, "Spatial Evolution of Laser Beam Profiles in an SBS Amplifier," *Appl. Opt.* **28**, 92–96 (1989).

G. J. Rickard, A. R. Bell, and E. M. Epperlein, "2D Fokker-Planck Simulations of Short-Pulse Laser-Plasma Interactions," *Phys. Rev. Lett.* **62**, 2687–2690 (1989).

M. L. Tsai, S. H. Chen, and S. D. Jacobs, "Optical Notch Filter Using Thermotropic Liquid Crystalline Polymers," *Appl. Phys. Lett.* **54**, 2395–2397 (1989).

Forthcoming Publications

S. Augst, D. Strickland, D. D. Meyerhofer, S. L. Chin, and J. H. Eberly, "Tunneling Ionization of Noble Gases in a High Intensity Laser Field," to be published in *Physical Review Letters*.

S. H. Batha, D. D. Meyerhofer, and A. Simon, "Enhanced Scattering from Laser-Plasma Interactions," to be published in *Physical Review*.

B. Boswell, D. Shvarts, T. Boehly, and B. Yaakobi, "X-Ray Laser Beam Propagation in Double-Foil Targets," to be published in *Physics of Fluids*.

P. C. Cheng, V. H-K. Chen, H. G. Kim, and R. E. Pearson, "A Real-Time EPI-Fluorescent Confocal Microscope," to be published in the *Journal of Microscopy*.

P. C. Cheng, V. H-K. Chen, H. G. Kim, and R. E. Pearson, "An EPI-Fluorescent Spinning-Disk Confocal Microscope," to be published in the *Proceedings of the 47th Annual Meeting of Electron Microscopy Society of America (EMSA)*, Austin, TX, 14–18 August 1989.

J. M. Chwalek, D. R. Dykaar, J. F. Whitaker, R. Sobolewski, S. Gupta, T. Y. Hsiang, and G. A. Mourou, "Ultrafast Response of Superconducting Transmission Lines," to be published in *Ultrafast Phenomena VI*.

J. M. Chwalek, D. R. Dykaar, J. F. Whitaker, T. Y. Hsiang, G. A. Mourou, D. K. Lathrop, S. E. Russek, and R. A. Buhrman, "Picosecond Transient Propagation Studies on Thin-Film Y-Ba-Cu-O Transmission Lines," to be published in *Ultrafast Phenomena VI*.

W. R. Donaldson, "Picosecond and Femtosecond Laser Systems for Particle Accelerator Applications," to be published as a Brookhaven Report.

W. R. Donaldson, A. M. Kadin, P. H. Ballentine, and M. Shoup III, "Optically Activated High Temperature Superconductor Opening Switches," to be published in the *Proceedings of the 7th IEEE Pulsed Power Conference*, Monterey, CA, 11–14, June 1989.

D. R. Dykaar, R. Sobolewski, and T. Y. Hsiang, "Picosecond Switching Dynamics of a Josephson Tunnel Junction," to be published in *Ultrafast Phenomena VI.*

M. Y. Frankel and T. Y. Hsiang, "Picosecond Transient Behavior of Pseudomorphic High Electron Mobility Transistor–Simulations," to be published in *IEEE Transactions on Electron Devices.*

M. Y. Frankel, D. R. Dykaar, T. Y. Hsiang, K. H. Duh, and P. C. Chao, "Non-Invasive, Picosecond Transient Characterization of Pseudomorphic High Electron Mobility Transistor (HEMT)," to be published in *IEEE Transactions on Electron Devices.*

R. L. McCrory, "Energy Supply and Demand in the Twenty-First Century," to be published in the *Journal of Fusion Energy.*

R. L. McCrory, "Progress and Plans for Inertial Confinement Fusion at the University of Rochester," to be published in *Journal of Fusion Energy.*

R. L. McCrory and C. P. Verdon, "Computer Modeling and Simulation in Inertial Confinement Fusion," to be published in *Il Nuovo Cimento.*

R. L. McCrory, J. M. Soures, C. P. Verdon, S. Skupsky, T. J. Kessler, S. A. Letzring, W. Seka, R. S. Craxton, R. Short, P. A. Jaanimagi, M. Skeldon, D. K. Bradley, J. Delettrez, R. L. Keck, H. Kim, J. P. Knauer, R. L. Kremens, and F. J. Marshall, "Laser Compression and Stability in Inertial Confinement Fusion," to be published in *Plasma Physics and Controlled Fusion.*

Conference Presentations

W. R. Donaldson, "Ultrafast High Power Switching: Techniques and Applications," presented at Electro '89, New York, NY, 11–13 April 1989.

The following presentations were made at the CLEO '89 Conference, Baltimore, MD, 24–28 April 1989:

W. Donaldson, P. Ballentine, and A. Kadin, "Electrical Switching in Superconducting YBCO Thin Films Using Picosecond Optical Pulses."

T. Kessler, S. Letzring, S. Skupsky, M. Skeldon, S. Morse, and P. Jaanimagi, "Broadband Phase Conversion of the Frequency Tripled OMEGA Laser."

L. E. Kingsley and W. R. Donaldson, "Two-Dimensional Electro-Optic Imaging."

J. C. Lee, S. D. Jacobs, T. J. Kessler, and N. Van Lieu, "Profile Tunable Laser Beam Apodizer."

M. Pessot and G. Mourou, "Amplification of 100 fsec Pulses in Alexandrite Using Chirped Pulse Techniques."

W. Seka, S. Morse, S. Letzring, R. Kremens, T. Kessler, P. Jaanimagi, R. Keck, C. Verdon, and D. Brown, "Power Balancing of Multi-Beam Laser Fusion Lasers."

M. J. Shoup III and J. H. Kelly, "A High-Energy, Short-Pulse, Multiwavelength, Slab-Geometry Nd:Phosphate Glass Laser Source."

M. D. Skeldon, T. Kessler, R. S. Craxton, S. Skupsky, W. Seka, and J. M. Soures, "Efficient Third-Harmonic Generation with a Broadband Laser."

A. L. Gaeta, M. D. Skeldon, and R. W. Boyd, "Observation of Instabilities of Laser Beams Due to the Brillouin Interaction."

The following presentations were made at the QELS '89 Conference, Baltimore, MD, 24–28 April 1989:

S. Augst, D. Strickland, S. L. Chin, J. H. Eberly, and D. D. Meyerhofer, "High Intensity Multiphoton Ionization Experiments at 1053 nm and 527 nm."

H. E. Elsayed-Ali, "An Ultrahigh Vacuum Laser-Driven Picosecond Diffraction Facility."

T. B. Norris, G. A. Mourou, N. Vodjdani, B. Vinter, C. Weisbuch, X. J. Song, and L. F. Eastman, "Time-Resolved Studies of Tunneling in Single and Double Quantum Well Structure."

S. Uchida, M. C. Richardson, H. Chen, Y. Chuang, P. A. Jaanimagi, D. D. Meyerhofer, B. Yaakobi, and R. S. Marjoribanks, "Picosecond Laser Plasma X-Ray Source."

A. Lindquist, S. D. Jacobs, and V. Plotsker, "Chemo-Mechanical Prepolish of Phosphate Laser Glass for Reducing Subsurface Damage," presented at the American Society for Precision Engineering (ASPE) Conference on Sub-Surface Damage in Glass, Tucson, AZ, 25–27 April 1989.

M. Pessot, J. Squier, G. Mourou, and D. J. Harter, "Amplification of 100 fsec mJ Pulses in Alexandrite Using Chirped Pulse Techniques," presented at the Tunable Solid State Laser Meeting, Cape Cod, MA, 1–3 May 1989.

The following presentations were made at the IEEE International Conference on Plasma Science, Buffalo, NY, 22–24 May 1989:

T. Boehly, B. Yaakobi, R. S. Craxton, R. Epstein, M. C. Richardson, M. Russotto, D. Shvarts, J. M. Soures, and J. Wang, "Recent Developments in X-Ray Laser Research at LLE."

G. G. Luther, C. J. McKinstrie, and R. W. Short, "The Filamentation of Two Counterpropagating Waves."

J. Wang, T. Boehly, B. Yaakobi, D. Shvarts, R. Epstein, D. Meyerhofer, M. C. Richardson, M. Russotto, and J. M. Soures, "Analysis of Multiple-Foil XRL Targets Using X-Ray Spectroscopy."

C. J. McKinstrie and G. G. Luther, "The Modulational Instability of Linear Waves," presented at Spring College on Plasma Physics, International Center for Theoretical Physics, Trieste, Italy, 22–26 May 1989.

The following presentations were made at the Seventh IEEE Pulsed Power Conference, Monterey, CA, 11–14 June 1989:

W. R. Donaldson, A. M. Kadin, P. H. Ballentine, and M. Shoup III, "Optically Activated High Temperature Superconductor Opening Switches."

L. E. Kingsley and W. R. Donaldson, "Electro-Optics Surface Field Imaging System."

J. F. Whitaker, J. A. Valdmanis, T. A. Jackson, K. A. Bhasin, B. Romanofsky, and G. A. Mourou, "External Electro-Optic Probing of Millimeter-Wave Integrated Circuits," presented at the 1989 IEEE Microwave Theory and Techniques Symposium, Long Beach, CA, 12–13 June 1989.

T. Y. Hsiang, J. F. Whitaker, R. Sobolewski, S. Martinet, and L. P. Golob, "High-Frequency Characterization of Superconducting Transmission Structures from Picosecond Transient Measurements," presented at the International Superconductive Electronics Conference, Tokyo, Japan, 13 June 1989.

M. Guardalben, A. Schmid, S. Jacobs, and S. H. Chen, "1054-nm Damage Thresholds for Monomeric and Polymeric-Side-Chain Liquid Crystal Systems," presented at the U.S. Army Science Symposium on Nonlinear Optical Polymers, Natick, MA, 13–14 June 1989.

C. Immesoete, L. Forsley, and H. Kim, "Computer-Assisted Microballoon Selection For Laser Fusion Targets," presented at the Forth Conference, Rochester, NY, 19–23 June 1989.

The following presentations were made at the 19th Annual Anomalous Absorption Conference, Durango, CO, 19–23 June 1989:

S. H. Batha, D. D. Meyerhofer, and A. Simon, "Comparison of Enhanced Thomson Scattering from Long and Short Scale-Length Plasmas."

T. Boehly, D. Bradley, and J. Delettrez, "Shine-Through Early-Time Phenomena in Laser Fusion Targets."

Y-H. Chuang, S. H. Batha, H. Chen, D. D. Meyerhofer, M. C. Richardson, and S. Uchida, "Characterization of Plasmas Produced by Intense, 1-ps, Laser Pulses."

R. S. Craxton, "X-Ray Laser Emission from Long Line-Focus Plasmas."

J. Delettrez, D. D. Meyerhofer, and M. C. Richardson, "Hydrodynamic Simulations of Ultrashort Laser Pulse Interaction."

E. M. Epperlein, "Enhanced Laser Penetration and Self-Focusing in Large Scale Underdense Plasmas."

R. Epstein and S. Skupsky, "Anticipated Improvement in Laser Beam Uniformity Using Distributed Phase Plates with Quasi-Random Patterns."

R. L. Keck, W. D. Seka, S. Letzring, S. Morse, and J. M. Soures, "Improvements to Energy and Power Balance on OMEGA."

G. G. Luther, C. J. McKinstrie, and R. W. Short, "The Filamentation of Two Counterpropagating Waves."

C. J. McKinstrie, "The Relativistic Modulational Instability of Light Waves in Rarefied Plasma."

D. D. Meyerhofer, Y-H. Chuang, J. Delettrez, and M. C. Richardson, "Calculation of Inverse Bremsstrahlung Absortion of High-Intensity Laser Light in Short Scale Length Plasmas."

W. Seka, R. L. Keck, S. Letzring, S. Morse, and J. M. Soures, "Energy, Power Balance, and Irradiation Uniformity on OMEGA."

R. W. Short, "Stimulated Raman Scattering in the Caustic Illumination Sheath Surrounding a Laser Fusion Target."

A. Simon, "Numerical Studies of X-Ray Emission by Fast Electron Pulses."

S. Skupsky, R. W. Short, T. Kessler, R. S. Craxton, S. Letzring, and J. M. Soures, "Improved Laser-Beam Uniformity Using the Angular Dispersion of Frequency-Modulated Light."

The following presentations were made at the conference on Super-Intense Laser-Atom Physics, Rochester, NY, 28–30 June 1989:

S. Augst, D. Strickland, S. L. Chin, J. H. Eberly, and D. D. Meyerhofer, "Multiphoton Ionization of Noble Gases in the Tunneling Limit."

D. D. Meyerhofer, S. Augst, S. L. Chin, J. H. Eberly, and Q. Su, "High Order Harmonic Generation Using the Tabletop Terawatt Laser."

ACKNOWLEDGMENT

The work described in this volume includes current research at the Laboratory for Laser Energetics, which is supported by Empire State Electric Energy Research Corporation, New York State Energy Research and Development Authority, Ontario Hydro, the University of Rochester, and the U.S. Department of Energy Office of Inertial Fusion under agreement No. DE-FC03-85DP40200.